Experimental Study: Foam Generation and Propagation in Flow Across a Permeability Contrast

Herru As Syukri (4610628)

Delft University of Technology

TU Delft Delft University of Technology

Challenge the future

Experimental Study: Foam Generation and Propagation in Flow Across a Permeability Contrast

Herru As Syukri
Student ID : 4610628

in partial fulfillment of the requirements for the degree of

Master of Science
in Applied Earth Sciences

at the Delft University of Technology
to be defenced on Thursday, August 30, 2018

Supervisors:

Prof. Dr. W. R. Rossen,	Delft University of Technology
S. Shah. Msc,	Delft University of Technology

Thesis Committee:

Prof. Dr. W. R. Rossen,	Delft University of Technology
Dr. K. H. A. A. Wolf,	Delft University of Technology
Dr. A. Askarinejad,	Delft University of Technology
S. Shah. Msc,	Delft University of Technology

Cover photo taken at Duri Steamflood Field, Indonesia

Abstract

Foam is useful as an enhanced oil recovery method to reduce gas mobility and prevent gravity override to improve sweep efficiency. Foam is generated in porous media when exceeding a critical velocity and pressure gradient, that usually occur near to an injection well. There is the uncertainty of foam generation in the low-pressure gradient and velocity further from the injection well. However, foam can be generated at such a permeability change with no minimum pressure gradient or superficial velocity. In field application, permeability contrasts originate from cross-bedding in fluvial sand-channel reservoirs, reservoir layering, and sharp heterogeneity changes over a few centimeters to kilometers of the formation.

This study describes series of experiments with various of gas fractional flows, and injection velocities. The experiments use synthetic sintered glass porous media to create consolidated nature of porous medium with a sharp boundary between low- and high-permeability layers. The experiments are augmented by the medical X-ray computerized tomography (CT) machine, which can be used to generate dynamic images of the core flood.

This study proves that capillary snap-off plays a dominant role in foam generation across a sharp heterogeneity boundary (low to high permeability) regardless of the superficial injection velocity that is applied in the system. In our experiments, as the injection velocity reduced, the magnitude of pressure fluctuations increase. Across the permeability jump, as the injection velocity reduces, the observed pressure gradient during foam generation is also higher. However, foam is difficult to propagate at very low injection velocity, in our case 0.17 ft/day (0.025 ml/min). These conditions observed at sintered glass core with permeability contrast 3.8:1 (0.17 ft/day and 80% of foam quality) and permeability contrast 14:1 (0.17 ft/day and 95% of foam quality). In terms of gas fractional flow, the CT results verify the pressure gradient profile at different gas fractional flow experiments (60%, 80%, and 95%), foam is indeed generated at the permeability contrast and propagates downstream to the outlet of the core.

Keywords: *Foam generation; permeability contrast; injection velocity; fractional flow; capillary snap-off*.

Acknowledgments

All praises to Allah for the strengths and His blessing in completing this thesis.

I would like to express my grateful thanks to my principal supervisor Prof. Bill Rossen for the opportunity to join on this project. He had always allocated his time to share the knowledges, give the advices and feedback during thesis process. I would like to thank my direct supervisor Swej Shah, for his patience supervision and guidance in the experiments and writing of this thesis.

Furthermore, I would also thank to Michiel Slob, Marc Friebel, Karel Heller, Ellen Meijvogel-de Koning, Jolanda van Haagen-Donker, and Joost van Meel for their technical support at the Laboratory of Geo-science and Engineering of Delft University of Technology

I would like to express my gratitude to Dr. Karl-Heinz Wolf and Dr. Amin Askarinejad as committee members for spending their valuable time to review, and evaluate the thesis.

I would also like to thank The Indonesian Endowment Fund for Education (Lembaga Pengelola Dana Pendidikan) for the the scholarship during my study at TU Delft.

Herru As Syukri
Delft, August 2018

Contents

List of Figures

List of Tables

1

Introduction

Enhanced oil recovery is a technique to produce the oil that remains in a reservoir after primary and secondary recovery. Primary recovery utilizes pressure as the main driving force to produce the fluids: solution gas drive, water drive, and gas cap drive. Also, artificial lift supports fluid flow to the surface. The purpose of secondary recovery is mainly to maintain reservoir pressure by injecting water or gas.Tertiary oil recovery is a technique to increase oil production by the injection of materials not commonly present in the reservoir (Lake *et al.* 2014). It consists of mainly three methods: thermal, chemical, and gas injection (Table 1.1).

Chemical injection involves polymer injection to improve the volumetric sweep of water flooding by reducing water mobility, or using a surfactant to reduce surface tension, allowing trapped oil droplets to flow. Thermal recovery heats up the reservoir to reduce the viscosity of the oil and allow oil flow through the reservoir. The purpose of gas injection to dissolve and displace oil in the reservoir by injecting N_2 or CO_2, whether or not the gas develops miscibility with oil. Volumetric

Table 1.1: *Oil Recovery Classification*

Primary Recovery	Natural Flow	Conventional Recovery
	Artificial Lift (Pump/Gas Lift)	
Secondary Recovery	Waterflood	
	Gas Reinjection	
Tertiary Recovery	Thermal	Enhanced Recovery
	Chemical	
	Gas Injection	

sweep efficiency measures the effectiveness of an enhanced oil recovery process, especially during gas injection EOR, in maximizing the volume of oil contacted with displacing fluid divided by the volume of target oil. Early breakthrough in gas

injection EOR results in poor sweep efficiency (Figure 1.1). It happens due to gravity segregation of gas to the top of the reservoir, fingering due to the lower viscosity of gas compared to oil and water, or channeling of a higher mobility fluid through regions of higher permeability (Lake *et al.* 2014).

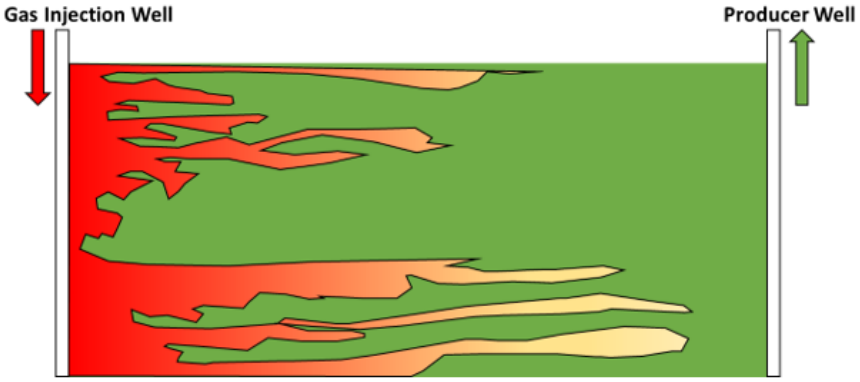

Figure 1.1: *Schematic of an early breakthrough in gas injection. Red is the gas phase, and green is the liquid saturation. Fingering and channeling usually occur in gas injection EOR because gas has lower viscosity, and density than liquid and gas tends to flow through the layer with higher permeability.*

1.1. Foam in Gas Injection EOR

The oil and gas industry utilizes foam as an additive for drilling fluid to allow under-balanced drilling operation, lubricate the bit and carry cuttings to the surface (Rossen 1996). Another function of foam is for acidizing or fracturing the rock matrix to divert acid or fracturing fluid. This study focuses on the use of foam in porous media for enhanced oil recovery by reducing gas mobility and preventing gravity override and channeling, thereby improving sweep efficiency.

Foam in porous medium is a dispersion of gas in liquid such that the liquid phase is interconnected and at least some of the gas flow paths are blocked by lamellae (Rossen 1996). Foam generation in the porous medium is a change of state from relatively high gas mobility to low gas mobility. Microscopically, strong foam generation occurs when the rate of lamella creation is significantly higher than lamella destruction. Conversely, limited lamella creation or instable lamellae result in weak foam (Gauglitz *et al.* 2002). Several studies (Gauglitz *et al.* 2002, Ransohoff and Radke 1988, Tanzil *et al.* 2002a) show that strong foam is generated in a homogeneous porous media by exceeding a critical pressure gradient (or injection velocity). This condition usually occurs in the near-borehole region. However, there is the uncertainty about foam generation and propagation at the low-pressure gradient and low-velocity further from the injection well.

Other studies (Ransohoff and Radke 1988, Falls *et al.* 1988, Rossen 1999, Tanzil *et al.* 2002b) show that foam can be generated by snap-off when liquid

and gas flow across the sharp boundary from lower to higher permeability. In field application, permeability contrasts originate from cross-bedding in fluvial sand channel reservoirs in layered reservoirs, and at sharp heterogeneities over a few centimeters to kilometers of the formation.

If foam generation were independent of the pressure gradient in a heterogeneous formation with low superficial velocity, it would improve the chances of success of a foam application, as it would entail gas mobility reduction deep inside the reservoir.

1.2. Objectives of Study

The aim of this study is as follows: Study foam generation due to flow across a sharp permeability heterogeneity by performing a series of experiments over a wide range of injection conditions; study the effect of gas fractional flow and injection velocity on foam generation at the sharp heterogeneity; and examine foam generation and propagation with dynamic saturation maps obtained by X-ray Computerized Tomography (CT) scans.

1.3. Outline of Thesis

The organization of this thesis as follows: Chapter 2 contains a detailed introduction to the behavior of foam in porous media, including the fundamental mechanism of foam generation at permeability contrast, with a discussion of previous experimental studies of foam generation. Chapter 3 describes the experimental design and methodology. Chapter 4 describes experimental results outlining the effect of foam quality, superficial velocity and permeability contrast on foam generation. Chapter 5 provides the discussion, and Chapter 6 contains conclusions from the study and recommendations for future work.

2

Theoretical Background

2.1. Fundamentals of Foam in Porous Media

A low recovery factor in gas EOR (Enhanced Oil Recovery) injection may be primarily due to poor sweep efficiency, as the gas contacts and sweeps only small portion of the reservoir. Major causes of poor sweep efficiency are gravity segregation, fingering due to an unfavorable mobility ratio, and high mobility gas channeling at greater permeability. Foam can improve sweep efficiency by reducing the effect of reservoir layering and low gas viscosity. There are two types of subsurface applications concerning foam in porous media: plugging and mobility control (Rossen 1996). In the plugging process, foam can be used to selectively plug the high-permeability layers, allowing the displacing fluid to contact the unswept, low-permeability zones. The more ambitious goal of using foam in subsurface application is field-wide mobility control to optimize macroscopic displacement.

Foam is an agglomeration of gas bubbles separated from each other by a thin liquid film or lamella (Bikerman 1973). There are two types of foam in porous media (Figure 2.1). The first is continuous-gas foam, where at least one gas channel is connected. The liquid lamellae block the flow of gas in one part of the pore space and gas flows through another part of the pore space without displacing these lamellae. The second type is discontinuous-gas foam, where lamellae block all pathways, and no channels are available for gas to flow. Gas flow occurs only once lamellae move, and a macroscopic pressure gradient must provide the energy required to displace lamellae.

If two phases (liquid and gas) are present in the pore space, the permeability of the porous medium to one phase decreases due to the presence of the other phase. The relative permeability of phase i, which is a function of the saturation of phase i, represents the effective reduction in permeability, as shown in Equation 2.1:

$$u_i = -\frac{kk_{ri}}{\mu_i}\frac{\Delta P}{L} = -(\lambda_i)\nabla P \tag{2.1}$$

where λ_i is mobility of phase i (m^2/Pa.s), u_i is superficial velocity of phase i (m/s), k is absolute permeability of the rock (m^2), k_{ri} is relative permeability of phase i, ∇P is pressure gradient of phase i (Pa/m), and μ_i is viscosity of phase i (Pa.s).

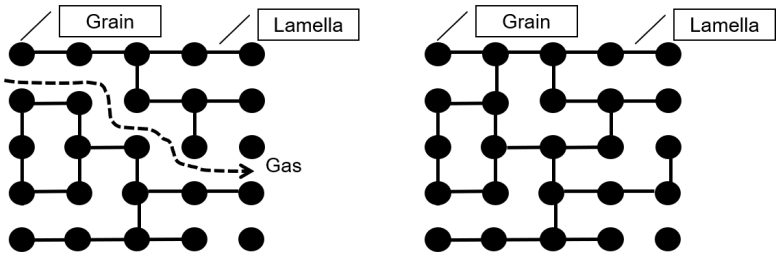

Figure 2.1: *(right) Continuous gas-foam (left) discontinuous gas-foam, modified from (Rossen 1996).*

Mobility λ_i in equation 2.1 depends on permeability (rock property), relative permeability (a function of phase saturation, wettability and rock type), and viscosity (fluid property). Reducing gas relative permeability and increasing gas viscosity can reduce the high mobility of gas. Discontinuous gas-foam not only reduces gas relative permeability but also leads to larger gas viscosity. On the other hand, continuous gas-foam reduces only the gas relative permeability.

In an experiment, it is hard to separate the effects of viscosity and relative permeability in the reduction of gas mobility, because both are affected by foam in a complicated way. Drag on bubble flow increases the viscosity and gas trapping results in the reduction of gas relative permeability. The gas relative permeability increases again if there is a sufficiently large pressure gradient to transport the lamella across the pore space. Mobility reduction factor (R) and effective gas viscosity (μ_g^{eff}) quantify the gas mobility reduction:

$$\mu_g^{eff} = \mu_g R \tag{2.2}$$

where μ_g is gas viscosity. A high value of R means a large reduction of mobility (strong foam) and small R values represent weak or coarse foam.

2.2. Foam Generation in Porous Media

Foam generation creates numerous lamellae or liquid films that separate the gas bubbles. There are three primary mechanisms of foam generation in porous media: leave-behind, lamella division, and snap-off.

Leave-Behind - Figure 2.2 illustrates how the leave-behind mechanism creates lamellae in the throat between pore bodies when gas invades the pore space initially saturated with surfactant solution. Leave-behind occurs only during drainage, when non-wetting phase (gas) enters the pore space. This mechanism is one reason that foam generation is easier to achieve in drainage than during imbibition or simultaneous gas-liquid flow.

Snap-off - Snap-off occurs when gas invades a pore throat, and then liquid accumulate in the throat, eventually bridging and blocking the throat (Falls *et al.*

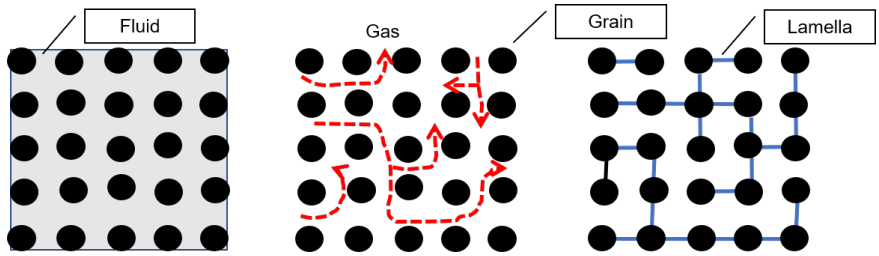

Figure 2.2: *(Left) Initial state saturated with a surfactant; (Middle) Gas invasion through pore space; (Right) Leave behind lamellae. Modified from (Rossen 1996).*

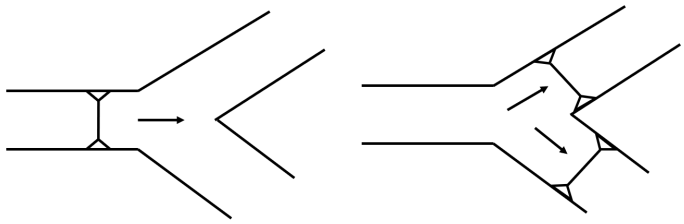

Figure 2.3: *Lamella divide at a pore branch*

1988, Rossen 1988). Initial gas entry to the pore requires that capillary pressure be higher than capillary entry pressure (P_c^e). Following gas entry, the snap-off mechanism requires that capillary pressure in the pore throat then fall to value that low enough (P_c^{sn}) to cause liquid to flow back into the pore throat and form a lamella. The value of P_c^{sn} depends on geometry of pore throats (Rossen 1996). Experimental result of Falls *et al.* (1988) for bead-packs shows that critical capillary pressure for capillary snap-off is about ½ the capillary entry pressure of porous medium ($P_c^{sn} = P_c^e/2$).

There are several mechanisms by which capillary pressure can fall by a factor of 2 from P_c^e to P_c^{sn} as required for snap-off. This thesis focuses on the 4^{th} mechanism of snap-off in the study of Rossen (2003): there is a narrow region of low capillary pressure in steady liquid-gas flow across sharp permeability contrast. Several experimental studies show lamella creation in flow at a transition in flow from low permeability to high permeability (Ransohoff and Radke 1988, Falls *et al.* 1988, Tanzil *et al.* 2002b). In the extreme case, snap-off happens at the outlet face of a porous medium due to the capillary end effect.

Lamella Division - Lamella division is a secondary generation mechanism, and it requires that some lamellae be present in the porous medium. When a lamella enters a pore body with several pore throats, it breaks or deposits a new lamella in each pore throat. Figure 2.3 shows a single lamella dividing into two lamellae.

2.3. Foam Generation in Homogeneous Porous Media

Some experimental studies observe that there is a minimum velocity (v^{min}) or pressure gradient (∇P) for foam generation in homogeneous porous media (Gauglitz *et al.* 2002, Ransohoff and Radke 1988, Tanzil *et al.* 2002a). Foam generation is an abrupt change of state from high gas mobility to low gas mobility, or a transition from "no foam" or "weak foam" into "strong foam". Weak foam can be thought of as a foam of high gas mobility due to unstable lamellae or rapid destruction of lamellae (Gauglitz *et al.* 2002). The transition to strong foam requires a period where the rate of lamella creation exceeds the rate of lamella destruction. Figure 2.4 shows the foam generation at fixed injection rate occurs as a sudden increase in pressure drop across the core.

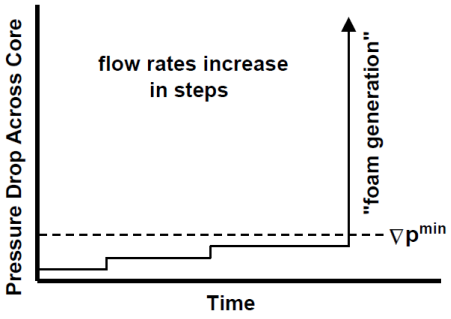

Figure 2.4: *Minimum pressure gradient for foam generation at a fixed flow rate (Gauglitz et al. 2002). Increase in pressure drop upon foam generation.*

In the study of Tanzil (2001), above a critical capillary number (N^*_{cL}) value equal to 2, there is strong foam generation in homogeneous media as shown at Equation 2.3:

$$N_{cL} = \frac{\Delta P}{\left(\frac{\sigma}{\sqrt{k/\phi}}\right)} \tag{2.3}$$

where ΔP is pressure drop across the system (Pa), σ is surface tension (N/m), ϕ is the porosity (-), and k is the absolute permeability (m^2).

2.4. Foam Generation in Heterogeneous Porous Media

Foam generation occurs in flow across a sharp increment in permeability. The pore-network model study of Rossen (1999) shows that snap-off occurs at a sharp permeability increase. During drainage through the low-permeability region, capillary pressure must be at a certain value (P_{c1}) greater than the capillary entry

pressure (P_c^e). Liquid accumulates at the boundary in the low-permeability zone, causing the capillary pressure drop by a factor $\sqrt{k_2/k_1}$ to certain value of P_{c2}. Snap-off blocks throats with $(2\sigma/P_{c1}) \leq (\sigma/P_{c2})$. Foam generation due to capillary snap-off across sharp permeability increase requires $P_{c2} < P_{c1}/2$ and $k_2 \geq 4k_1$. The fractional flow of water f_w also constrains k_{rg}/k_{rw}:

$$f_w = (1 + \frac{k_{rg}}{k_{rw}} \frac{\mu_w}{\mu_g})^{-1} \tag{2.4}$$

where k_{rg}/k_{rw} is the ratio of relative permeabilities of gas and water, and μ_w/μ_g is the ratio of water to gas viscosity.

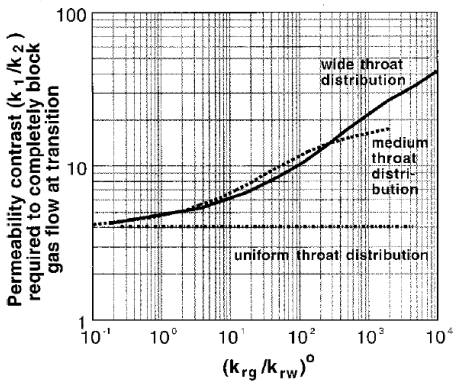

Figure 2.5: *Permeability contrast for foam generation by snap-off (Rossen 1999). This chart considers the calculation of equation 2.4*

Figure 2.5 shows the relation of liquid fractional flow (reflected in k_{rg}/k_{rw}) to the permeability contrast. For instance, if f_w=0.2 (foam quality = 80%) and water viscosity is 50 times than gas, equation 2.4 gives k_{rg}/k_{rw}=0.08 and requires a permeability contrast slightly above 4. At f_w=0.1, μ_w/μ_g=10 gives k_{rg}/k_{rw}=0.9. From Figure 2.5, at this fractional flow, a permeability contrast of 7:1 is required for snap-off. In summary, for foam generation in drier flow, a greater permeability contrast is required.

Schematically, Figure 2.6 explains the snap-off mechanism. During gas and liquid flow from low to high permeability, the saturation path follows from A to B to C (Yortsos and Chang 1990). If the change in permeability is abrupt, then there must be equilibrium across the boundary. Otherwise there is a discontinuity in pressure at the boundary. As a result, the capillary pressure decreases to P_c^{sn} in the low-permeability region just upstream of the boundary and snap-off happens. The capillary end effect gives a path from A to D to E, where the capillary pressure drops close to zero just outside the porous medium. This condition results in the increase of water saturation upstream of the end of the core. Figure 2.7 shows a schematic of the liquid saturation profile across a 1D domain with a sharp jump in permeability.

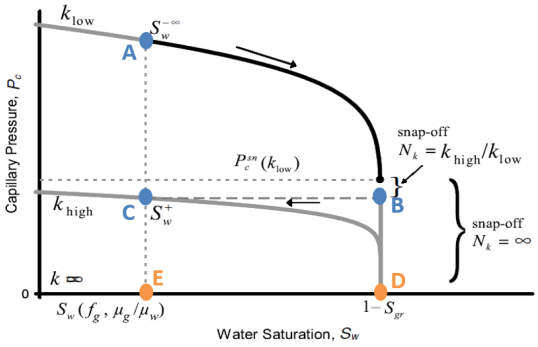

Figure 2.6: *The snap-off requirement for gas and liquid flow from low permeability to high permeability, modified from Tanzil et al. (2002b). See also figure 2.7.*

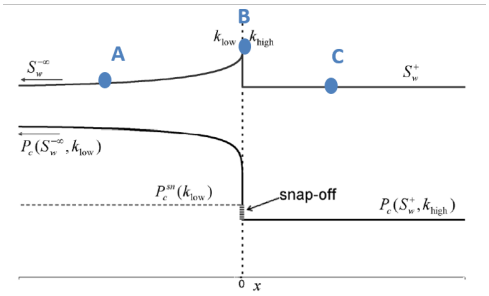

Figure 2.7: *Snap-off requirement for gas and liquid flow from low permeability to high permeability in spatial coordinates, modified from Tanzil et al. (2002b)*

To summarize, Rossen (1999) shows that snap-off can occur in flow across a sharp jump in permeability. Depending on the injected fractional flow, a minimum permeability contrast is required to observe the snap-off. At a higher gas fractional flow, a higher permeability contrast is required to observe foam generation. Tanzil *et al.* (2002b) extended the theory of Rossen (1999) to conclude that if the permeability jump is gradual, a higher permeability contrast is required for snap-off to occur given the same fractional flow, compared to a sharp jump in permeability. Figure 2.8 shows that the required permeability contrast may be greater if the permeability change is gradual rather than sharp because the occurrence of snap-off not only depends on permeability ratio and fractional flow but also on a capillary number of the transition region, $N_{c,trans}$.

2.5. Previous Experimental Study in the Heterogeneous Porous Media

Falls *et al.* (1989) performed a series of experiments measuring the capillary pressure required for snap-off in a sand-pack. In their experiments, they observed

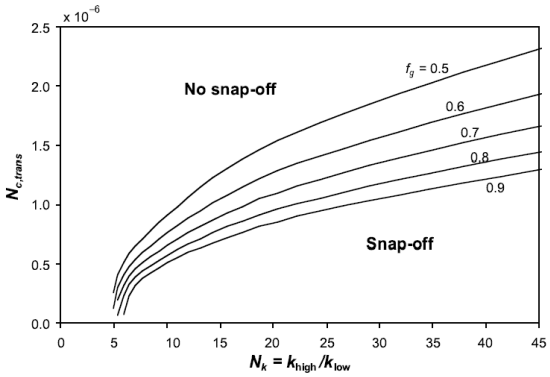

Figure 2.8: *The capillary number at transition-region for snap-off over permeability ratio (Tanzil et al. 2002b).*

that snap-off occurred at half of the capillary entry pressure. Additionally, they observed foam generation during the flow of gas into a pack initially filled with surfactant solution.

Tanzil *et al.* (2002b) conducted core-flood experiments using a sandpacks filled in a transparent tube, place horizontally, 1ft (30.5 cm) long and 1 in (2.54 cm) in diameter. The column consisted of 4 sections, the first and third sections were coarse sand of permeability 70 darcy, and the second and fourth sections were fine sand of permeability 16 darcy. The permeability ratio N_k was approximately 4.4:1 and injected gas volume fraction was fixed at 67%. All their experiments involved gas injection into a surfactant-saturated column (drainage). The section upstream of the permeability increase showed weak foam, and the strong foam was formed in the downstream high-permeability section. While the experiments of Tanzil and Falls showed foam generation in flow low- to high-permeability, they observed it during drainage. When gas drains a surfactant-saturated core, the foam can also have formed by leave-behind or "roof snap-off". Tanzil *et al.* (2002b) also examined the effect of gas fractional flow on the pressure-drop across the heterogeneous section (Figure 2.9). At gas fractional flow (fg) = 95%, the pressure-drop increased slowly, reflecting weaker foam. Strong, low-mobility foam, generated at fg = 67%, resulted in a much higher pressure-drop.

The experiments of Li *et al.* (2005) utilized vertical sandpacks of length 1 ft (30 cm) and diameter 0.84 in (2.05 cm). In the experiment, the sandpacks were set up vertically with injection from top to bottom. Initially, the core was saturated with brine followed by co-injection of brine and gas at a constant pressure until steady state was achieved. After that, co-injection of gas and surfactant was initiated at the same gas fraction. This procedure was followed to avoid gas draining a surfactant-saturated region during the foam-generation experiment. They did not observe foam generation in sandpacks with permeability ratios of 4.3:1 and 5.1:1, but they observed a significantly greater pressure gradient in sandpacks with permeability ratio 20:1. They reported that the failure to obtain strong foam in flow

across smaller permeability contrasts was due to inefficient packing near the walls of the sandpacks, resulting in a region of high porosity along the edges allowing gas bypass.

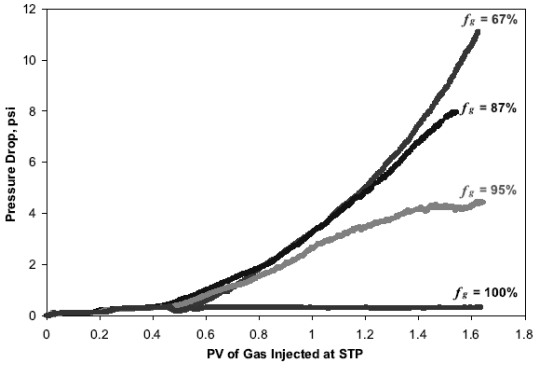

Figure 2.9: *Effect of gas fractional flow on the pressure drop across a sharp permeability (Tanzil et al. 2002a).*

2.6. Sharp Heterogeneities in Geological Formations

Grain size and sorting control the permeability of clastic reservoirs. Cross-bedding is one of the most common types of heterogeneity in reservoirs deposited under fluvial, tide-dominated and aeolian environments (Hartkamp-Bakker 1993). Fluvial channel sand bodies typically consist of stacked cross beds (Figure 2.10). Cross-bedding is layering within a stratum, at an angle to the main bedding plane. The contrast in grain size between individual foreset laminae and between adjacent foreset and bottom-set boundaries often results in sharp permeability contrasts within the sedimentary facies (Figure 2.11).

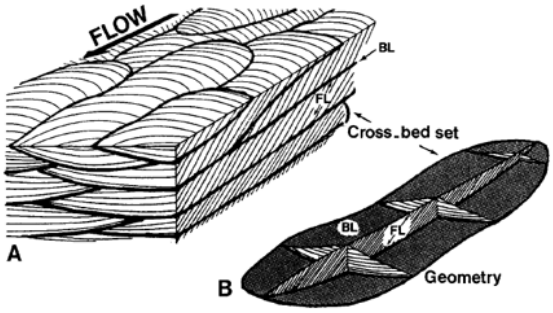

Figure 2.10: *(A) Vertically stacked cross beds with the unique bottom set (BL) and foreset (FS) facies. (B) Typical geometry of a cross bed set (Weber et al. 1982)*

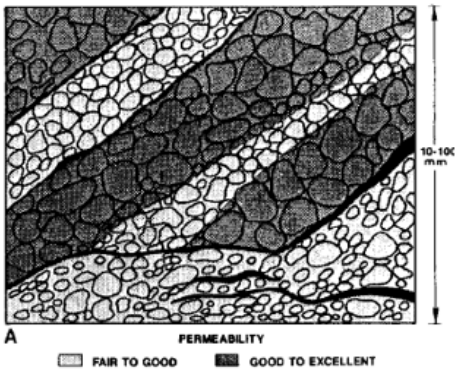

Figure 2.11: *Example of sedimentary-structure scale heterogeneity with part of the cross bed showing high- and low-permeability zones and clay in between individual foreset laminae (Ealey 1989)*

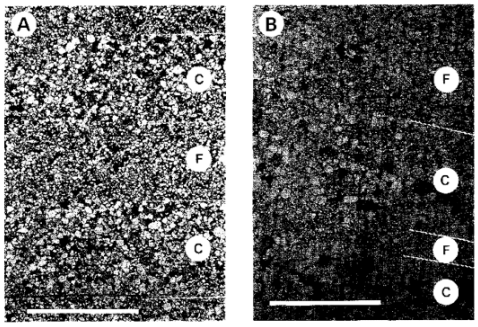

Figure 2.12: *Photomicrographs from thin sections of the Vollpriehausen sandstones. Laminated sample shows coarse-grained (C) and fine-grained (F) laminae. (Hartkamp-Bakker 1993)*

The measurement of Hartkamp-Bakker (1993) in the tertiary Loranca basin (central Spain) showed that permeability variation in the trough cross-bedding is proportional to grain size and sorting. In her measurements, the permeability in the bottom-set varied from 0.5-7 darcy and in the foreset from 5-17 darcy. Additionally, she analysed 23 core sections (with total 1939 data points) from a gas reservoir in the Dutch North Sea. The permeability contrast in the Upper Slochteren sandstone members and the Vollpriehausen sandstone members (Figure 2.12) varied between 1.7:1:1 (CFL:FFL:BL) and 27.9:9.6:1 (CFL:FFL:BL). Permeability contrast between fine-grained and coarse-grained foreset laminae varied between 1.3:1 (CFL:FFL) and 5.4:1 (CFL:FFL). Here, BL = bottom set layers, FFL = fine-grained foreset laminae, and CFL = coarse-grained foreset laminae.

3

Experimental Methodology and Material

3.1. Experimental Description

The objective of this study is to observe foam generation due to capillary snap-off in flow across sharp heterogeneities in a porous medium by performing a series of experiments over a wide range of injection conditions. The experiments utilize a sintered glass core to create uniform layers with a sharp transition between them. These experiments are performed at low injection velocities, close to field conditions (rule of thumb in the field = 1ft/day). The injection conditions that are varied in this study include fractional flow and injection velocity in core samples with different permeability contrasts. In addition, the experiments are augmented by X-ray computerized tomography (CT), which is used to generate dynamic saturation profiles during a core flood experiment.

3.2. Porous Media

This study utilizes a consolidated, synthetic, sintered glass core with a sharp permeability change (Figure 3.1). The core is manufactured by Hilgenberg GmbH, Malsfeld, Germany (www.hilgenberg-gmbh.de), made from pure borosilicate glass granules with a predetermined mesh size. Borosilicate glass is a type of glass with silica and boron trioxide as the main glass-forming constituents. The borosilicate granules are packed into a glass tube and sintered. Sintering is the process of compaction and consolidation through heat or pressure.

The low-permeability and high-permeability sections in the core are homogeneous. The lower-permeability section occupies roughly 1/3 of the pack and the higher-permeability section occupies the rest. Figure 3.2 shows the location of the pressure taps along the length of the core. Nylon tubes connect the pressure transducers to the glass walls of the porous medium. There are five pressure taps

connected to the core and two pressure taps outside the core measuring inlet and outlet pressure. This study reports a summary of experiments performed with three types of sintered glass cores having different magnitudes of permeability contrast. Table 3.1 highlights the specifications for every core used in this study.

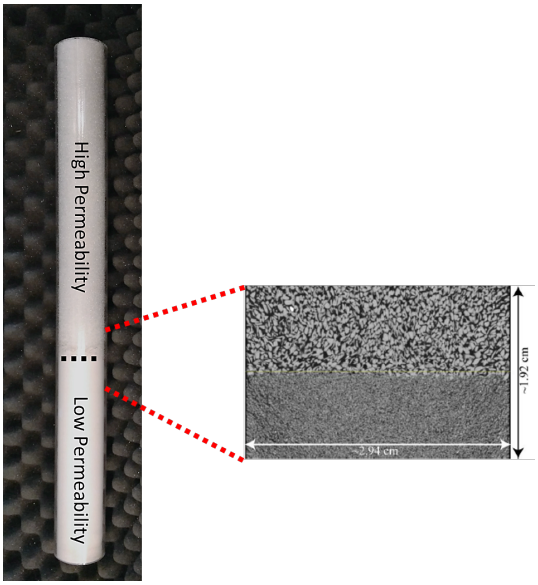

Figure 3.1: *(Left) Synthetic sintered glass core. (Right) microCT image across permeability contrast (Shah et al. 2018)*

Table 3.1: *Specifications of synthetic sintered glass cores*

	Core 1		Core 2		Core 3	
	Low-Perm Section	High-Perm Section	Low-Perm Section	High-Perm Section	Low-Perm Section	High-Perm Section
Pore size (µm) Specified by Manufacturer	16-40	40-100	40-60	100-160	16-40	100-160
Length (cm)	42		40.5		40	
Diameter (cm)	3		3		3	
Pore Volume (ml)	99.8		83.6		80.3	
Permeability (darcy)	5.26 D ± 0.029 D	20.70 D ± 0.08 D	10.25 D ± 0.043 D	50.03 D ± 0.412 D	5.13 D ± 0.054 D	70.15 D ± 0.02 D
Permeability Ratio	3.8:1		5:1		14:1	

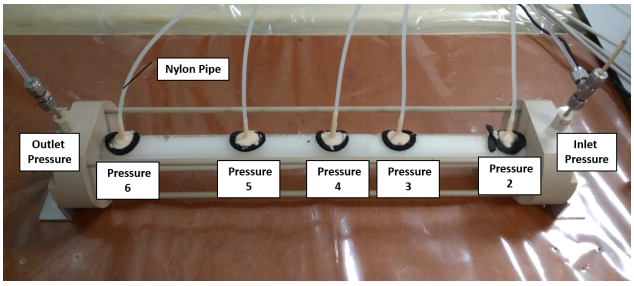

Figure 3.2: *Sintered glass core showing the location of five pressure taps connected to the core. Pressure is also measured before the inlet and after the outlet end-cap.*

3.3. Experimental Material and Setup

Material

The brine solution is 1.0 wt.% NaCl in demineralised water. 99.98% pure N_2 gas is injected at a fixed flow rate. The surfactant solution consists of 0.5 wt.% surfactant and 1.0 wt.% NaCl in demineralised water. The surfactant is anionic alpha olefin sulfonate (AOS) $C_{14\text{-}16}$ with a molecular weight of 315 g/mol (Bio-Terge AS-40 KSB). AOS has an outstanding detergency, lower adsorption on subsurface porous media, high compatibility with high-salinity water, and it is an excellent overall candidate for foam application in enhanced oil recovery project (Farajzadeh *et al.* 2008).

Setup

A Vindum pump (Number 4 in Figure 3.3) injects liquid (demineralised water, brine, or surfactant) into the core. Any liquid solution injected is degassed before injection. This is done to avoid any gas from being trapped in the pump housing during operation. Degassing the injected liquid also ensures that no gas comes out of solution inside the core, altering the gas fractional flow. The Vindum fluid pump (Model VP-12K-HC) has two cylinders; fluids are injected through Nylon tubing of 1/8 inch OD connecting the glass core to the pump and mass flow controller through a T-junction. Nitrogen is injected through the Bronkhorst mass-flow controller (Number 6 at Figure 3.3) that has a maximum flow rate of 0.7 ml/min and operating pressure 10 bar. The FlowView application controls the flow rate based on a percentage of maximum flow rate.

Five pressure taps are drilled through the acrylic glass that covers the sintered glass core. Nylon tubing connects the core to Keller pressure transducer (Number 3 at Figure 3.3). The Keller pressure transducer (type PA-33x) has a pressure range from -1 bar to 6 bars to measure absolute pressure. There is no back-pressure regulator in this experiment, to avoid any fluctuation in pressure due to multiphase flow through it. Since we operate at atmospheric pressure and the pressure drop across the system is low (as shown later in Chapter 4), gas-compression effects are negligible.

The surface tension is measured using a tensiometer with the Du Noüy–Ring

method. This equipment consists of a rod with a small ring that is made from a composite metal material (Platinum-Iridium). Before the measurement, the rod is cleaned with water and heated under a naked jet flame to remove impurities. The rod is hung in the thin metal hook and the Du Noüy–Ring method measures the maximum pull force when the ring is first immersed into the solution and then slowly pulled out from the interface. Before measuring the surface tension of the liquid sample, we need to calibrate the tensiometer using water. The surface tension is measured according to the following equation:

$$\sigma = \frac{F}{L.\cos\theta} \tag{3.1}$$

where F = force maximum when the ring moves through the interface, L = the length of the ring, i.e. the sum of the inner and outer circumference, and θ = contact angle between the ring material and liquids.

Computed-tomography (CT) scanning (Figure 3.5) uses X-rays to build cross-sectional images or slices through the body. Then, the cross-section is reconstructed from the measurement of the attenuation coefficient of X-ray beams in the volume of the object. Computed tomography allows for 3D reconstruction of density within any object. In this experiment, the CT scan result is valuable for porosity and 2-phase saturation measurement. Table 3.2 shows the imaging settings used in this experiment:

Specification	Core 1	Core 2
Tube Voltage (kV)	140	140
Tube Current (mA)	250	250
Slice Thickness (mm)	1.5	0.6
Time (second)	8.95	18.59
Image Reconstruction Kernel	B50f medium sharp	B50f medium sharp

Table 3.2: *Setting of CT scan Measurement*

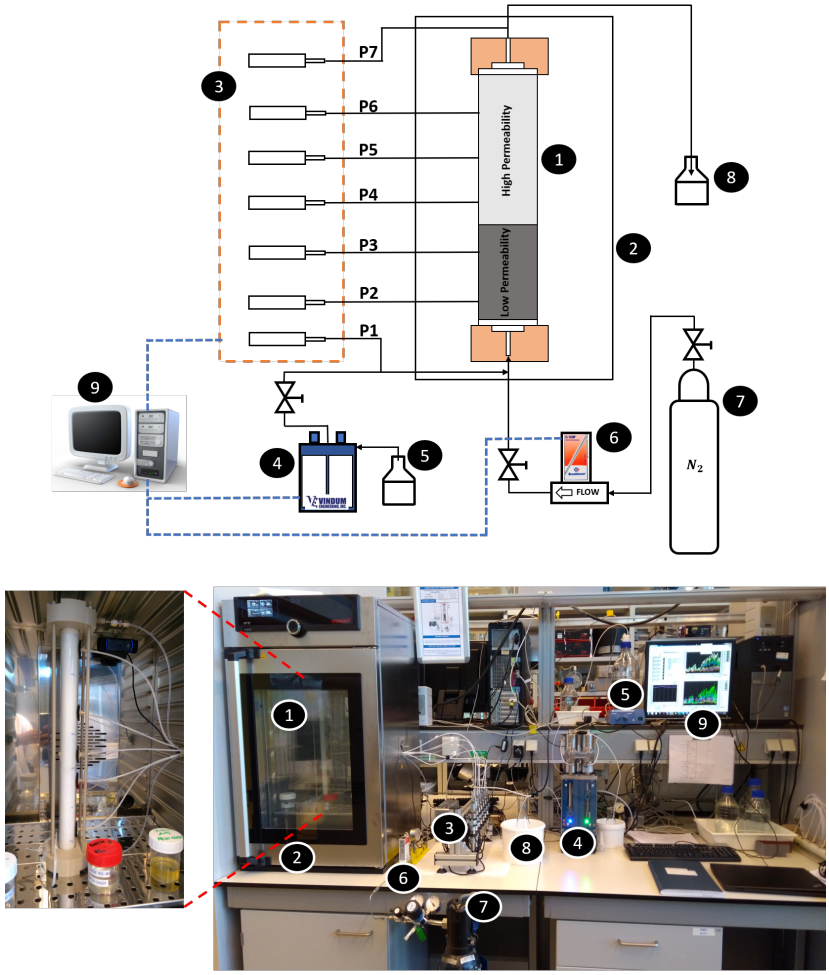

1	Sintered Glass Core
2	Lab Oven
3	Pressure Transducer
4	Liquid Pump (Vindum Eng)
5	Liquid Bottle
6	Mass-flow Controller (Bronkhorst)
7	Gas Tank
8	Outlet Bottle
9	Data Acquisition

Figure 3.3: *(Upper Image) Schematic of a experimental setup, (Lower Image) Experimental apparatus.*

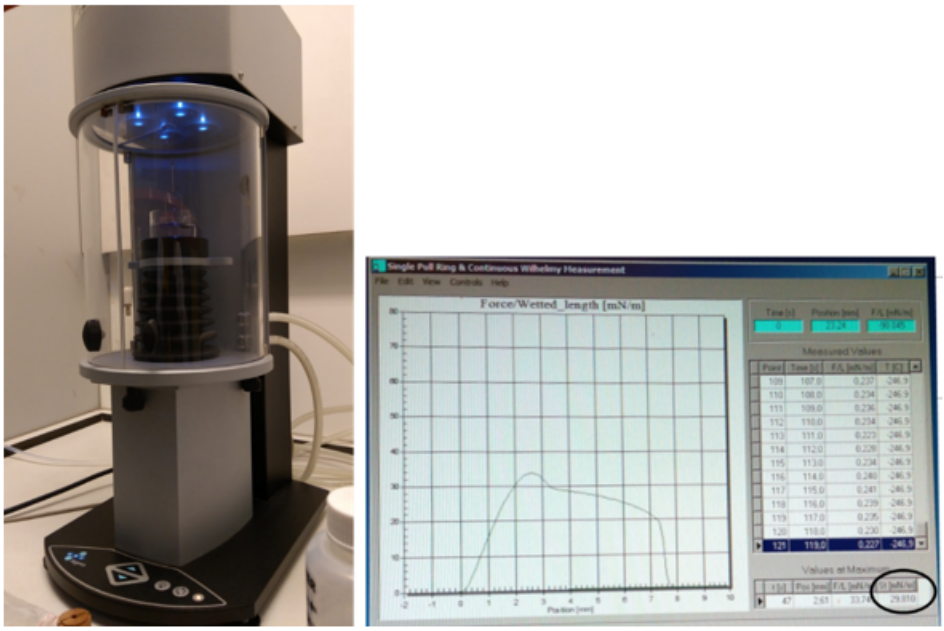

Figure 3.4: *(left) Tensiometer. (right) The result of surface tension measurement.*

Figure 3.5: *Computed Tomography (CT) Scanner, in this photograph set up for two cores.*

3.4. Experimental Procedure

The procedures consist of pore-volume measurement, permeability measurement, main experiment and cleaning procedure after the experiment.

3.4.1. Pore-Volume Measurement

There are two methods to measure pore volume in this experiment:

- **Ideal-gas method**. After ensuring that the core is in a dry condition, we measure the pore volume by N_2 injection into the core at a specific flow rate with the outlet is closed. Pressure rise over time can be related to the incremental moles of N_2 injected into the core using the ideal gas equation as shown below:

$$PV = nRT$$

$$\frac{dP}{dt}V = \frac{dn}{dt}RT$$

$$V = \frac{\frac{dn}{dt}RT}{\frac{dP}{dt}} \tag{3.2}$$

where dn/dt is the number of moles injected per unit time (mol/s), R is the ideal gas constant (L bar K^{-1} mol^{-1}), T is temperature (K), dP/dt is the change in pressure over time (bar/s), Q is flow rate (L/s), and V_m is the volume molar (L/mol). The values of V_m and R are shown at table 3.3. Pore volume value from this calculation is subtracted by dead volume (volume of inlet line to the core and outlet from the core) to achieve actual pore volume of the core.

Table 3.3: *Known value for pore volume measurement*

R (ideal gas constant)	V_m
$8.314\ 10^{-2}$ L bar K^{-1} mol^{-1}	24.79 L/mol at 25^0C

- **CT scan method**. CT data is obtained throughout the volume of a scanned object in Hounsfield units (HU). Using the CT data obtained by scanning a dry porous medium and a liquid-saturated porous medium, the porosity of the porous medium can be calculated as follows (Sharma *et al.* 1997, Simjoo 2012):

$$\phi = \frac{CT_{wm} - CT_{am}}{CT_w - CT_a} \tag{3.3}$$

where ϕ is Porosity, CT_{wm} is the CT attenuation of a water-saturated core (HU), CT_{am} is the CT attenuation of a dry core (HU), CT_w is the CT attenuation of water in bulk (HU), and CT_a is the CT attenuation of air in bulk (HU).

3.4.2. Permeability Measurement

Permeability is measured using water and brine. The brine solution consists of degassed water + 1 wt.% NaCl. First, CO_2 is injected into the core to displace any light gases. Next, the core is vacuumed to remove CO_2. While vacuuming the core, degassed water is injected until it appears in the vacuum chamber at the outlet of the core (Number 8 at Figure 3.3). Then, the outlet is closed and pressure is allowed to build-up until the system pressure rises above atmospheric pressure. At this point, the core is fully saturated with nearly-incompressible water. Sharp jump in pressure with changes in flow rate reflect that this is indeed the cause. Next, the pressure transducers are zeroed under no-flow conditions in a water-saturated system. Permeability is measured by recording pressure gradient in various sections of the core across a wide range of flow rates as shown in Figure 3.6. Permeability

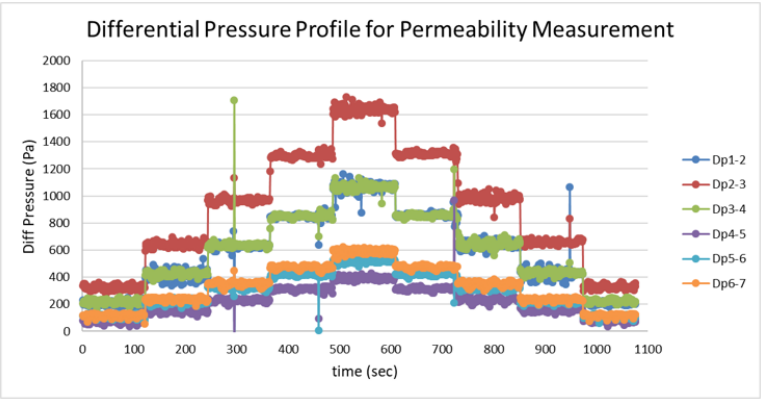

Figure 3.6: *Differential pressure for permeability measurement.*

is calculated using Darcy's law as:

$$\frac{q}{A} = k\frac{\Delta P}{L\mu} \tag{3.4}$$

q / A is plotted against $\Delta P/L\mu$ to achieve absolute permeability as the slope of a straight line passing through the measured points and the origin. Here, q (m^3/s) is the flow rate, k (m^2) is the absolute permeability, μ (Pa-s) is liquid viscosity, ΔP(Pa) is differential pressure, A (m^2) is the cross section of core and L (m) is the length of the core. Figure 3.7 shows a sample linear regression used to obtain the absolute permeability value.

3.4.3. Main Experiment (Foam Generation and Propagation)

Before conducting co-injection of gas and brine, the core is initially saturated with brine as part of the permeability-measurement routine. The desired value of gas and liquid fraction to be injected is set through the mass flow controller and Vindum pump software, respectively. First, co-injection of brine and gas commences to form a baseline for pressure measurements and to establish an initial

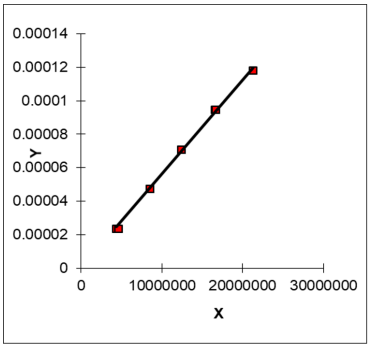

SLOPE, Permeability	5.62E-12	m^2
confidence intervals = 95%		
slope, beta1	7.97E-14	m^2

Figure 3.7: *Linear regression to obtain absolute permeability value. The table on the right-hand side contains the value of permeability and the 95% confidence interval for the linear regression.*

condition that ensures that initial foam generation is not triggered by drainage. To indicate the arrival of gas into a particular section of the core, the pressure transducers show abrupt jumps in pressure. Once co-injection of brine and gas reaches steady state, surfactant solution and brine are injected simultaneously. The LabView application is used to display most experimental measurements such as the absolute pressure, differential pressure, and temperature as shown in Figure 3.9. The Vindum Pump-Control (Figure 3.10) application records the flow rate and cumulative liquid injected, and the FlowView application controls the gas flow rate. We expect that no foam generates in the low-permeability section. Instead, foam starts to generate across the sharp permeability contrast and propagates through the high-permeability section to the end of the core. In this thesis, we conduct a series of experiments as shown in table 3.4.

A series of experiments are performed over a wide range of injection conditions in order to examine the effect of injected gas fractional flow and injection velocity on foam generation. The main measurement in all the experiments is pressure gradient, computed using seven pressure-taps connected to the core, as shown in Figure 3.8. Pressure gradient across a section is computed as:

$$\nabla P_A = \frac{(P_u) - (P_d)}{L} \tag{3.5}$$

where ∇P_A is pressure gradient across section A (bar/m), P_u and P_d are the gauge pressures measured through ports upstream and downstream, repectively, of section A (bar), and L is length of section (m). Since foam is generated in the high-permeability section of the core, apparent viscosity is computed in that section to quantify the reduction in gas mobility as:

$$\mu_{g,app} = \frac{k^H}{u_g + u_l} \nabla P \tag{3.6}$$

where k^H is absolute permeability in the high-permeability zone (m^2), u_g is injection

velocity of gas (m/s), u_l is injection velocity of liquid (m/s), and ∇P is pressure gradient (Pa/m).

In this study, the core is placed vertically with the injection from bottom to the top of the core to prevent gravity segregation. However, the core is placed horizontally in all experiments performed in the CT scanner to ensure an accurate measurement of saturation in the core. The gantry of the CT scanner (source and receiver array) is designed for scanning cylindrical objects. The image reconstruction is also optimized for round or cylindrical objects. CT data, Hounsfield Unit (HU), from a scanned core is used to compute liquid saturation using the equation below (Sharma *et al.* 1997, Simjoo 2012):

$$S_{liq} = \frac{CT_{foam} - CT_{am}}{CT_{wm} - CT_{am}} \tag{3.7}$$

where S_{liq} is liquid saturation (-), CT_{foam} is the CT attenuation of experiment (HU), CT_{am} is the CT attenuation of the dry core (HU), CT_{wm} is the CT attenuation of a water-saturated core (HU).

Table 3.4: *Series of the Experiments*

No	Permeability Ratio	Injection Flow Rate	Injection Velocity	Gas Fractional Flow	Vertical/ Horizontal	Remarks
1	Core 3.8:1	0.1 ml/min	0.67 ft/day	80%	Vertical	
2	Core 3.8:1	0.075ml/min	0.5 ft/day	80%	Vertical	
3	Core 3.8:1	0.05 ml/mnt	0.33 ft/day	80%	Vertical	
4	Core 3.8:1	0.025 ml/mnt	0.17 ft/day	80%	Vertical	
5	Core 3.8:1	0.1 ml/min	0.67 ft/day	60%	Vertical	
6	Core 3.8:1	0.1 ml/mnt	0.67 ft/day	95%	Vertical	
7	Core 5.2:1	0.1 ml/mnt	0.67 ft/day	80%	Vertical	Foam in the inlet section
8	Core 5.2:1	0.05 ml/mnt	0.33 ft/day	80%	Vertical	Foam in the inlet section
9	Core 14:1	0.1 ml/mnt	0.67 ft/day	80%	Vertical	Foam in the inlet section
10	Core 14:1	0.025 ml/mnt	0.17 ft/day	95%	Vertical	
11	Core 3.8:1	0.1 ml/mnt	0.67 ft/day	80%	Horizontal	CT Scan
12	Core 3.8:1	0.1 ml/mnt	0.67 ft/day	60%	Horizontal	CT Scan
13	Core 3.8:1	0.1 ml/mnt	0.67 ft/day	95%	Horizontal	CT Scan
14	Core 5.2:1	0.1 ml/mnt	0.67 ft/day	80%	Horizontal	CT Scan. Foam in the inlet section
15	Core 5.2:1	0.1 ml/mnt	0.67 ft/day	95%	Horizontal	CT Scan. Foam in the inlet section

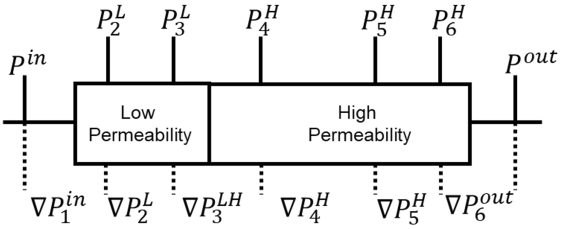

Figure 3.8: *Schematic of pressure tap along the core.*

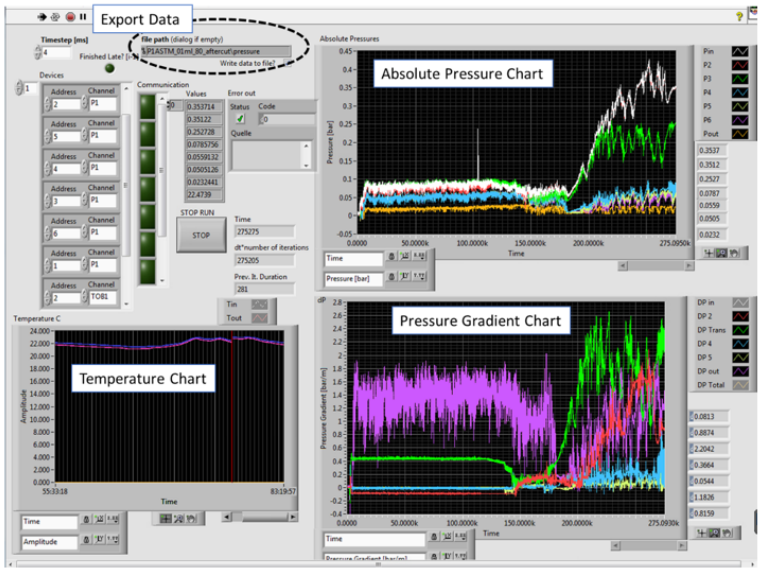

Figure 3.9: *LabView display. (Lower left corner) temperature data. (Upper right corner) absolute pressure data. (Lower right corner) Pressure-gradient data.*

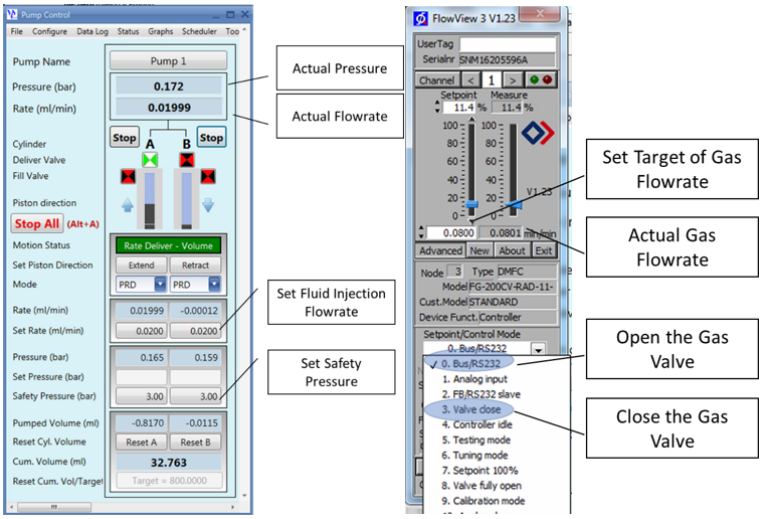

Figure 3.10: *(Left) Vindum application to control liquid injection. (Right) FlowView application to control gas injection from the Mass flow controller.*

4

Experimental Results

4.1. Summary

A summary of the results of foam-generation experiments together with subsequent analysis is presented in this chapter. A typical experimental observation is as follows. Figure 4.1a shows the gauge pressure and the pressure gradient (Figure 4.1b) as co-injection of gas and brine into a brine saturated core is initiated after the permeability-measurement step in the experimental procedure. As gas drains the low-permeability section, the inlet pressure (P_1^{in}) and the subsequent pressure measurement in low-permeability section (P_1^{in}, P_2^L, and P_3^L) rise, indicating the arrival of gas into the core (marked by no.1 in Figure 4.1a). This also corresponds to the blips in pressure gradient indicated by no.1 in Figure 4.1b.

Pressure gradient across the permeability transition stays at an unusually high level compared to the rest of the sections of the core as indicated by no.2 in Figure 4.1b. We think that this is due to the pressure transducers P_3^L and P_4^H sensing different phases. This effect has been observed in previous studies (McCool *et al.* 1983, Chen *et al.* 2016). At about 0.02 pore volumes of liquid injection (0.1 total pore volumes of injection or PVI), the pressure taps P_4^H, P_5^H and P_6^H indicate the arrival of gas. Gas breaks through the high-permeability zone very quickly as the pressure rise in all the taps connected to the high-permeability section occurs at nearly the same time, as seen in Figure 4.1a.

Following gas-brine co-injection, gas and surfactant solution are injected into the core and the pressure profile develops as shown in Figure 4.1a. Soon after, pressure gradient across the permeability jump shows a gradual decline as indicated by no.1 in Figure 4.2b. We think that this may be due to a dispersed surfactant front arriving at the pressure taps at permeability transition, gradually reducing the surface tension and therefore, the high pressure gradient which is a result of the transducers sensing different phases. This effect may also be explained, possibly in addition, by a reduction in local gas saturation near the pressure tap (P_3^L) due to a

lower surface tension. As the local gas saturation near the pressure tap drops, the local capillary pressure decreases. Numbers 2 and 3 in Figure 4.2b indicate a rise in pressure gradient across the high-permeability zones indicating foam generation across the permeability change and subsequent propagation through the given section towards the outlet of the core.

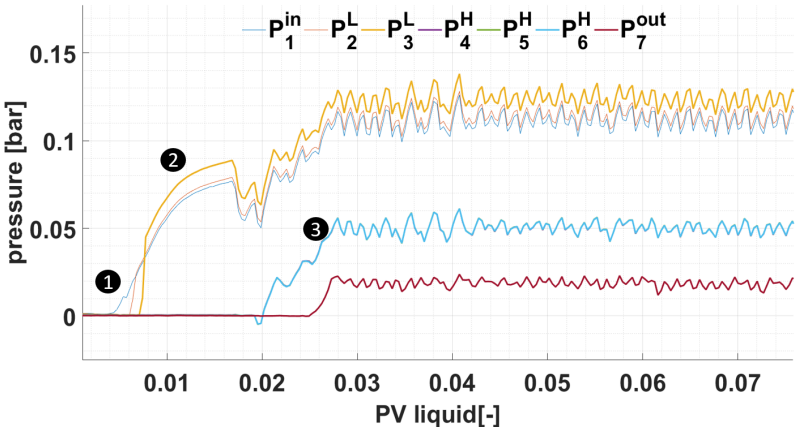

(a)

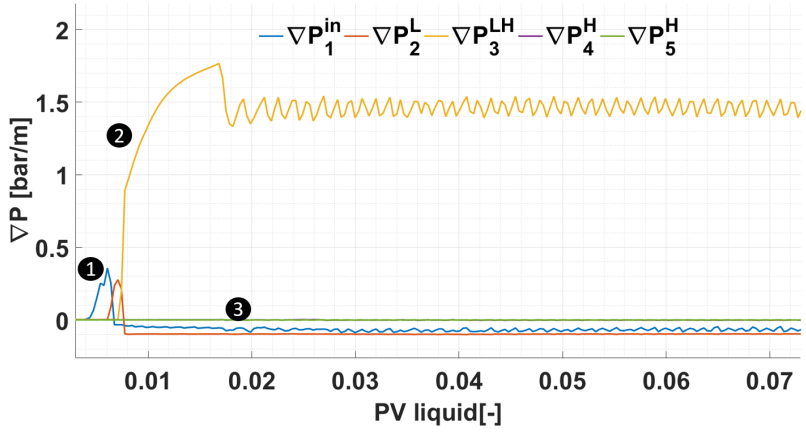

(b)

Figure 4.1: *Gauge pressure (**a**) and corresponding pressure gradient (**b**) versus pore volumes of liquid injection during gas-brine co-injection into a brine-saturated core.*

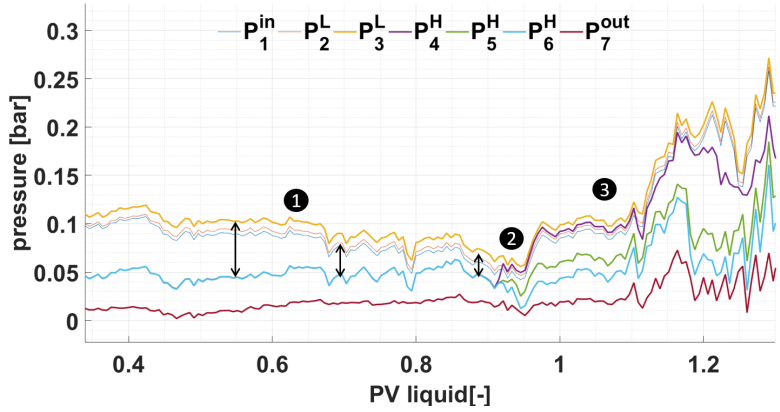

(a)

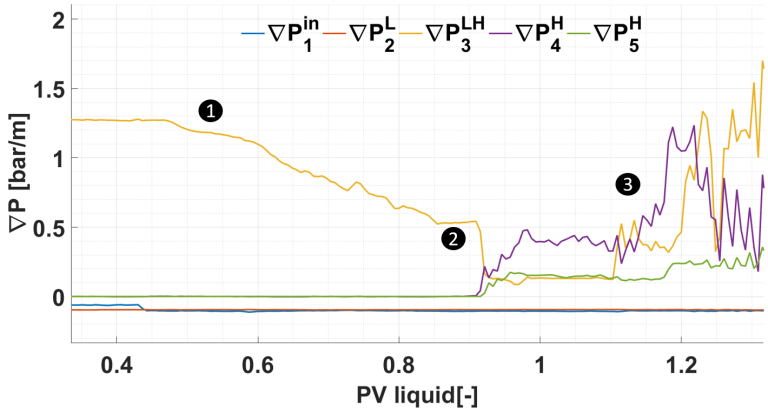

(b)

Figure 4.2: *Gauge pressure (**a**) and corresponding pressure gradient (**b**) versus pore volumes of liquid injection during gas-surfactant co-injection after steady steady gas-brine co-injection.*

4.2. Effect of Injection Velocity

In this section, the effect of injection velocity on the foam-generation process is reported. We performed experiments at four different velocities using Core 1 (permeability ratio 3.8:1): 0.67ft/day (0.1ml/min), 0.5ft/day (0.075ml/min), 0.33ft/day (0.05ml/min), and 0.17ft/day (0.025ml/min). The experiments are performed at a gas fractional flow of 80%, bringing the experimental conditions close to the critical conditions predicted for foam generation (Rossen 1999).

0.67ft/day (0.1ml/min). Figure 4.3 shows the pressure gradient across different section in core 1 at an injection velocity of 0.67ft/day (0.1ml/min) and fg=80%. At PVI = 0 (bottom left corner of the graph), injection of gas and

surfactant begins after gas-brine injection has reached steady state. As explained above, close to the time of arrival of the surfactant front at the permeability transition, ∇P_3^{LH} decreases gradually from 1.45 bar/m at 0.1 PVI surfactant (0.4 PVI total) to 0.5 bar/m at 0.4 PVI surfactant (2 PVI total). After 0.5 PVI surfactant (2.5 PVI total), the pressure gradient across the permeability contrast (∇P_3^{LH}) abruptly drops from 0.5 bar/m to 0.1 bar/m and at the same time pressure gradient downstream of the permeability contrast (∇P_4^{H}) rises to 0.1 bar/m. A significant rise in pressure gradient (∇P_4^{H}, ∇P_5^{H}) is observed at 0.7 PVI surfactant (3.5 PVI total), indicating foam propagation through the high-permeability zone.

0.5ft/day (0.075ml/min). Foam generation across the permeability jump is observed at a injection velocity of 0.5 ft/day (0.075 ml/min) with an injected gas fraction of 80%. As shown in Figure 4.4, the pressure gradient develops similar to the the experiment performed at 0.67 ft/day, showing foam generation at the boundary and subsequent propagation downstream. However, the pressure gradient across the high-permeability section of the core is higher at this lower velocity.

0.33ft/day (0.05ml/min). Figure 4.5 illustrates the pressure-gradient profile at a superficial velocity of 0.33ft/day (flow rate 0.05 ml/min). Once again, the pressure gradient through the course of the experiment develops in a similar manner. Interestingly, at this lower rate, the pressure gradient across the permeability transition and further downstream in the high-permeability section is noticeably higher, at about 1.2 bar/m. Moreover, the magnitude of fluctuations in the pressure gradients (∇P_3^{LH},∇P_4^{H}, ∇P_5^{H}) is significantly higher. This has to do with the unsteady nature of foam generation across the heterogeneity and its inherent intermittency (Shah *et al.* 2018).

0.17ft/day (0.025ml/min). Even at an extremely low injection velocity (compared to field values) of 0.17ft/day (qt=0.025 ml/min), the pressure-gradient profile reported in Figure 4.6 shows that foam was still generated due to flow across a sharp jump in permeability. This can be expected according to the theory of Rossen (1999), which suggests that this mechanism is independent of pressure gradient. However, in order to observe snap-off, there must be flow of gas and liquid across the permeability boundary, which is ensured, for practical purposes, by the small flow rate selected for this experiment. While foam is observed in the high-permeability section after roughly the same PVI, the pressure gradients (∇P_3^{LH},∇P_4^{H}) are much higher than those observed in experiments at higher velocities. The intermittency of foam generation across an abrupt permeability change is clearly demonstrated by the large magnitude of fluctuation in pressure gradient. The intermittency of foam generation (demonstrated by the magnitude of pressure fluctuations) increases as the flow velocity decreases. Intriguingly, the pressure gradient across the final section in the high-permeability region (∇P_5^{H}) is much lower (0.5 bar/m) than the previous three experiments shown in this section. This shows that the foam strength decreases as it propagates through the length of the high-permeability section. This is confirmed by observations made at the outlet of the core; relatively coarse foam (Figure 4.7b) followed by long periods

(over several PVI) of gas (Figure 4.7c) and liquid production (Figure 4.7d) are witnessed in the production tubing, in contrast to other experiments (Figure 4.7a) where typically foam is observed in the outlet tubing followed by short bursts of gas and liquid production.

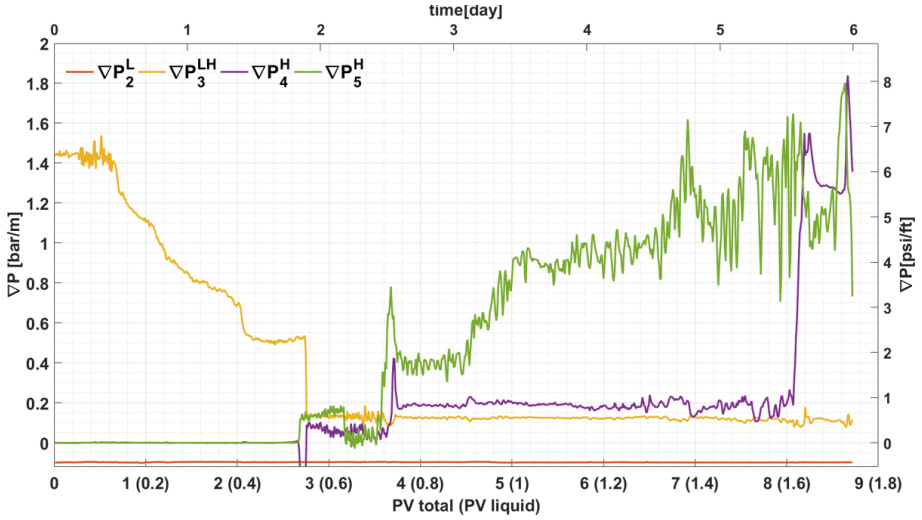

Figure 4.3: *Pressure gradient versus PVI for Experiment 1 conducted at vt = 0.67 ft/d (qt = 0.1 ml/min) and fg=80%.*

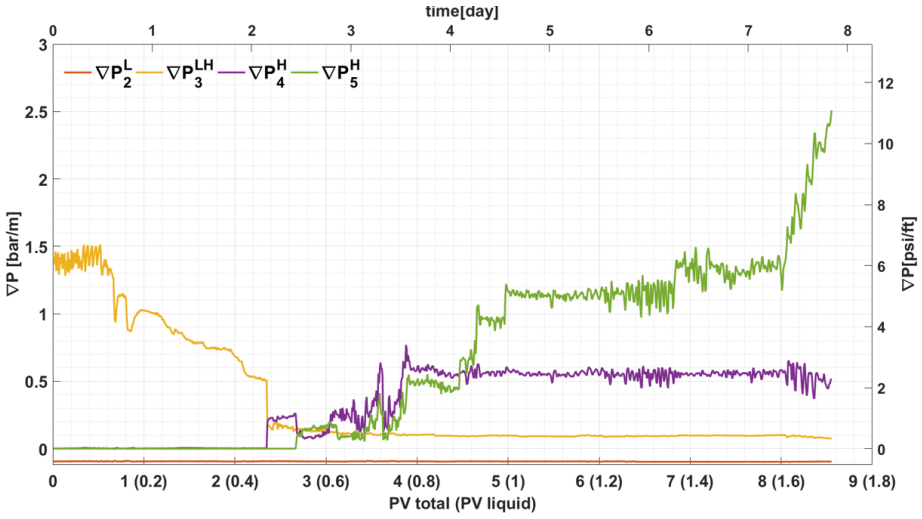

Figure 4.4: *Pressure gradient versus PVI for Experiment 2 conducted at vt = 0.5 ft/d (qt = 0.075 ml/min) and fg=80%.*

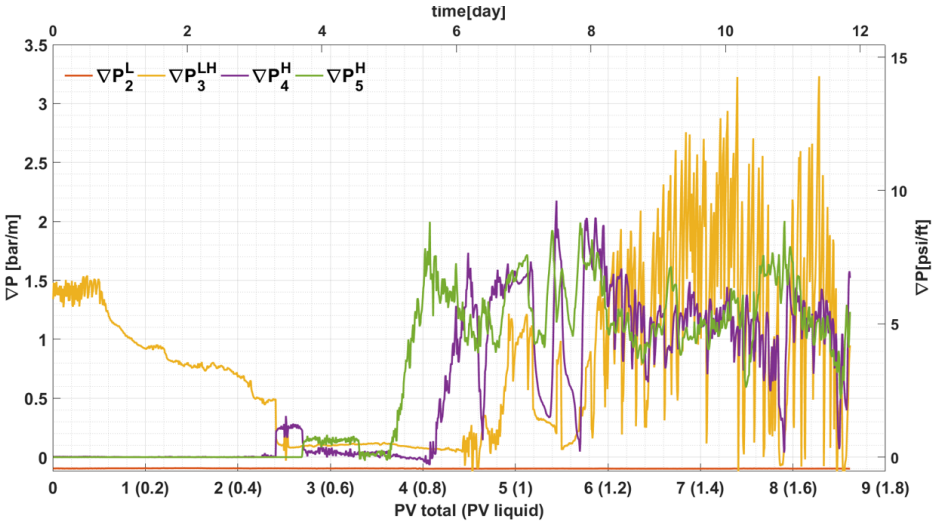

Figure 4.5: *Pressure gradient versus PVI for Experiment 3 conducted at vt = 0.33 ft/d (qt = 0.05 ml/min) and fg=80%. Noticeably, the magnitude of pressure gradient (∇P_3^{LH},∇P_4^H, ∇P_5^H) and the magnitude of fluctuation of these pressure gradients is higher than the two experiments reported above.*

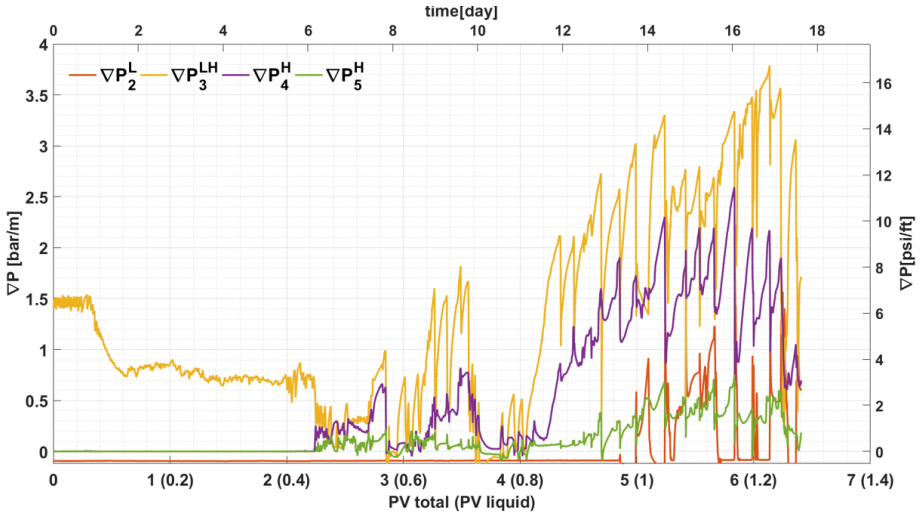

Figure 4.6: *Pressure gradient versus PVI for Experiment 4 conducted at vt = 0.17 ft/d (qt = 0.025 ml/min) and fg=80%. Distinct fluctuations in pressure gradient after approximately 3 PVI show the intermittency of this foam generation process. The magnitude of measured pressure gradient decreases from the transition to the outlet of the core, indicating that the foam weakens as it propagates through the high-permeability section.*

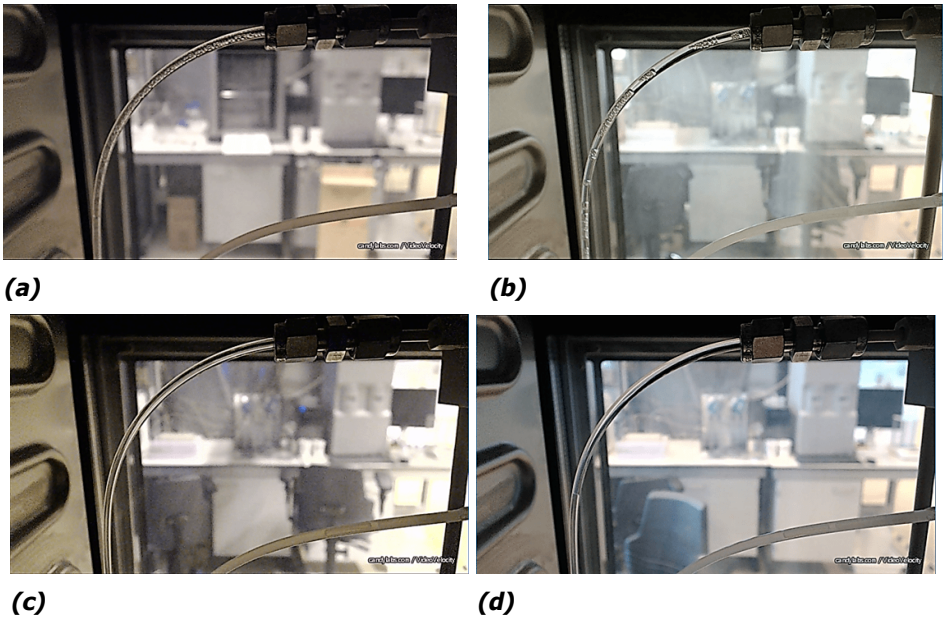

Figure 4.7: *Typical observation foam flow at outlet of the core at outlet for experiment 3 at injection velocity of 0.33ft/day (0.05ml/min) fg=80% at 4.5 PVI total (***a***), Typical observation of foam flow at outlet of core for experiment 4 at injection velocity 0.17ft/day (0.025ml/min) fg=80% 4.5 PVI total (***b***), Gas production after foam flow (***c***), Liquid production in the next day, roughly at 6 PVI total (***d***).*

4.3. Effect of Gas Fractional Flow

Core 1 is utilized to study the effect of gas fractional flow on foam generation across a sharp heterogeneity. In this series of experiments, total injection velocity is fixed at 0.67ft/day (qt=0.1ml/min) and injected gas fraction is varied from 60% to 95%. The experiments are augmented by X-ray computed tomography (CT), which is used to generate dynamic images of the core flood. The core is placed horizontally to obtain accurate scans and subsequent phase saturations profiles from the CT machine.

0.67ft/day (0.1ml/min) and 60% fg. Similar to the experiments reported in section 4.2, this experiment is performed in the CT scanner to study the effect of gas fractional flow with a high pressure gradient across the permeability change. For the experiment performed at fg = 60%, this is shown in Figure 4.8. The CT images whose scan times correspond to dashed lines in Figure 4.8 are shown in Figure 4.9. In Figure 4.10, 3-dimensional maps of the core showing phase saturation, particularly near the edges of the core, are presented at the same scan times. These images further help support the claim that high computed pressure gradient across the transition (∇P_3^{LH}) may be a result of P_3^L sensing the gas phase and P_4^H sensing the liquid phase.

As co-injection of surfactant solution and gas commences, a build-up in gas

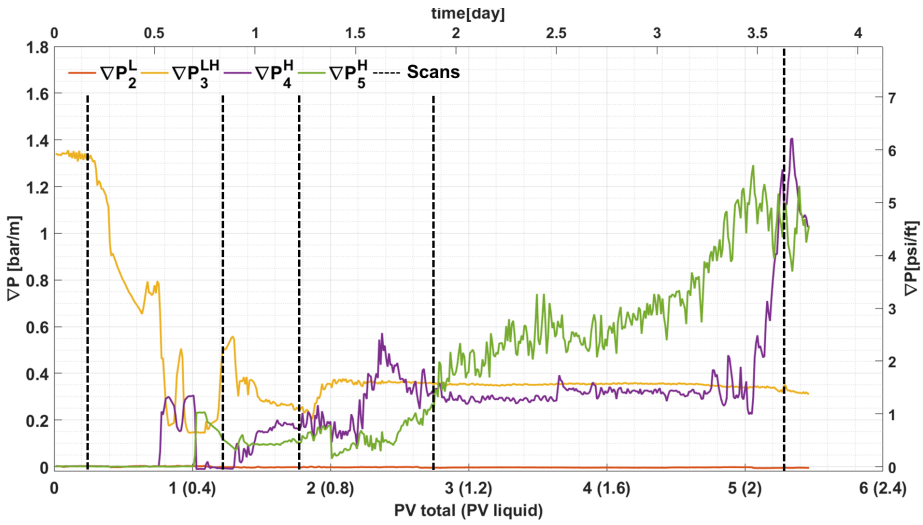

Figure 4.8: *Pressure-gradient profile at superficial injection velocity 0.67ft/day (qt=0.1ml/min) and fg=60%.*

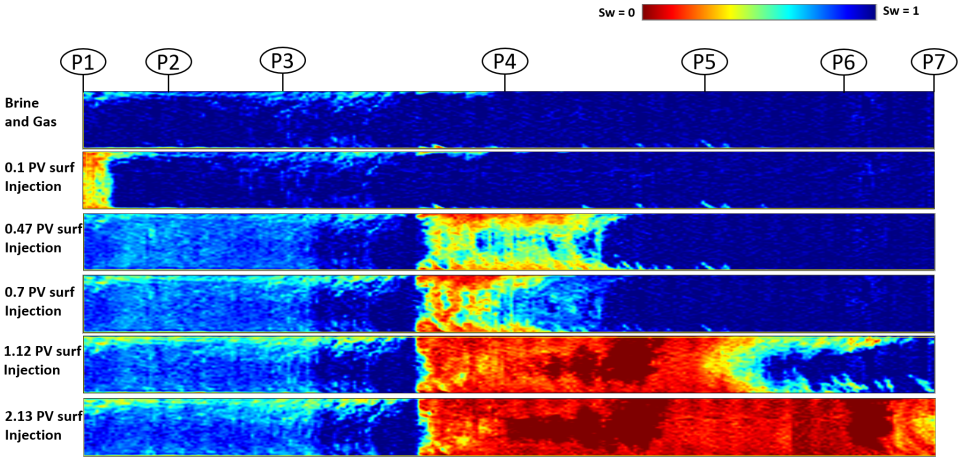

Figure 4.9: *2-Dimensional CT imaging in the center of the core as seen in vertical cross section. Blue illustrates as liquid saturation and red illustrates as gas saturation.*

saturation is observed near the inlet of the core as shown in the second image in Figure 4.9. This may be due to the formation of a weak or continuous-gas foam or due to the mobilization of trapped gas from the inlet end-cap due to the arrival of a lower interfacial-tension surfactant solution. It does not appear in the subsequent images and does not affect the process of foam generation observed later in our experiments.

Foam generation still occurs (at about 0.47 PVI liquid as shown in Figure 4.8)

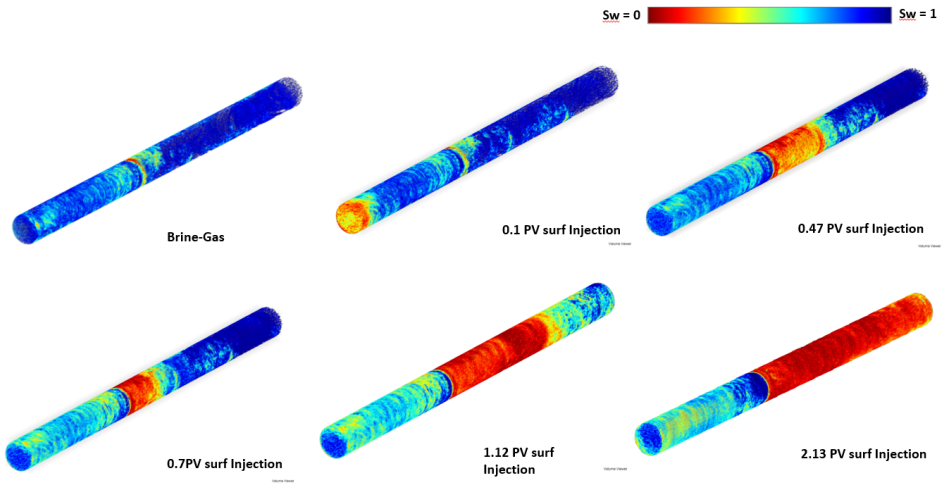

Figure 4.10: *3-Dimensional CT imaging at superficial injection velocity 0.67ft/day(qt=0.1ml/min) and fg=60%.*

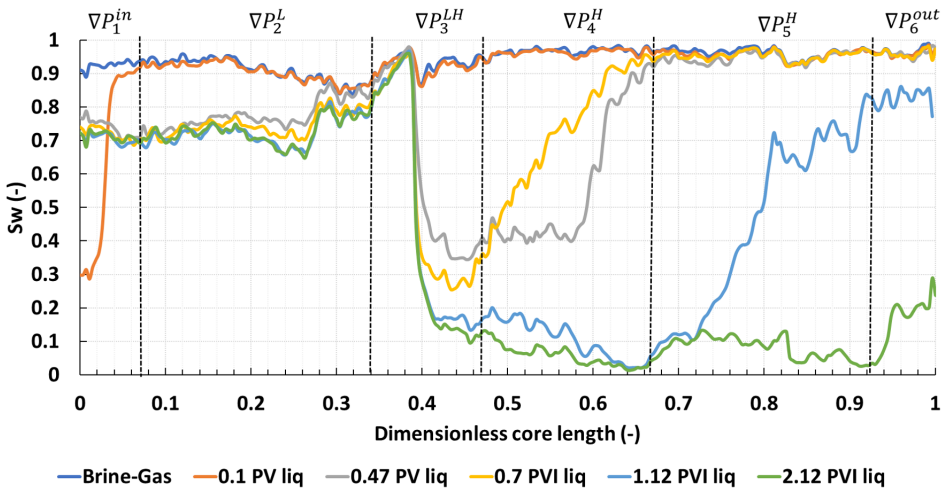

Figure 4.11: *Saturation profile along core section at injection velocity 0.67ft/day (0.1ml/min) and fg=60%.*

at the permeability transition as indicated by a build-up in gas saturation in the high-permeability zone near the boundary in the image at 0.47 PVI liquid in Figure 4.9. Figure 4.11 shows the saturation profile obtained by averaging phase saturations in each cylindrical slice across the length of the core. In this figure, at about 0.47 PVI surfactant, the high-gas-saturation front appears to be further

away than at 0.7 PVI surfactant. This is a result of the unwanted artefact of high porosity along the edges of sintered glass cores, which causes a larger amount of gas to flow along the walls of the core. Therefore, foam generation appears to begin near the edges of the core as shown as shown by a high gas saturation (red colour) in the image at 0.47 PVI surfactant in Figure 4.9. This reduction in gas mobility then results in a more uniform flow of gas across the entire face of the permeability transition causing foam generation throughout the circular cross-section of the core. Therefore, at 0.7 PVI surfactant, the gas saturation increases in the high-permeability zone but the foam front appears to have receded because the gas flowing along the edges, ahead of the foam front, in the image at 0.47 PVI surfactant has has bypassed the core through the edges of the pack and not contributed to the process of foam generation.

In the subsequent CT images at 1.12 PVI surfactant (2.8 PVI total) and 2.13 PVI surfactant (5.3 PVI total), foam appears to propagate through the high-permeability section. This is also evident in terms of pressure gradient as ∇P_4^H and ∇P_5^H begin to rise at around 0.8 PVI surfactant up until the end of the experiment as shown in Figure 4.8. The CT images confirm that foam is indeed generated at the permeability transition and there is no strong foam in the low-permeability zone affecting this process.

0.67ft/day (0.1ml/min) and 80%fg. At the beginning of this experiment, a relatively high gas saturation is observed in the low-permeability section as shown in the CT scan image at 0.2 PVI surfactant (Figure 4.13). Figure 4.14 shows a gas saturation of almost 75% in this region. However, there is no rise in pressure gradient in the low-permeability section of the core. This means that the higher gas saturation is not a result of large reduction in gas mobility, at least not to the extent that we expect to see with strong foam generation. Therefore, as explained above, this build-up in gas near the inlet is most likely due to the mobilisation of any trapped gas in the end-cap when surfactant is introduced in the system or due to the formation of a weak or continuous-gas foam that does not result in a significant mobility reduction. This build-up does not appear in the scan at 0.37 PVI (1.85 PVI total). At this point, the pressure gradient downstream of the permeability contrast (∇P_4^H and ∇P_5^H) starts to gradually increase as shown in Figure 4.12. Strong foam begins to be generated across the permeability contrast and appears in the CT scans at 0.68 PVI surfactant (3.4 PVI total). In Figure 4.14, liquid saturation clearly builds-up in the low-permeability zone near the permeability contrast to about S_w = 0.75, and drops abruptly in the high-permeability to about S_w = 0.2, reflecting an abrupt drop in gas mobility doe to foam generation across the permeability jump.

As seen in Figure 4.12, ∇P_4^H increases gradually from 0.2 bar/m at 0.7 PVI surfactant (3.5 PVI total) to 0.5 bar/m at 1 PVI surfactant (5 PVI total) reflecting foam propagation through the high-permeability section. A reduction in water saturation or increase in gas saturation can be seen in Figure 4.14 at 2.19 PVI surfactant due to foam propagation in the 4th section of the core (∇P_4^H). Then, indication of reduction in gas mobility due to foam propagation continues at 1.29 PVI surfactant (6.45 PVI total) until the end of experiment.

0.67ft/day (0.1ml/min) and 95%fg. In this experiment, we conduct

co-injection with a flow rate of 0.095 ml/min and 0.005 ml/min for gas and surfactant solution, respectively. Large fluctuations in pressure gradient across the permeability transition (Figure 4.15) after 0.13 PVI surfactant mark the onset of foam generation. The downstream pressure gradients ∇P_4^H and ∇P_5^H begin to rise, shortly after. Following foam generation and its appearance in the CT images, Figure 4.15 shows two distinct periods of high ($\approx$ 11-15 PVI total) and low ($\approx$ 15 PVI total till the end of the experiment) pressure gradient across the permeability transition. The scan taken in the high-pressure-gradient period corresponding to 0.68 PVI surfactant (13.6 PVI total) shows a build-up in gas saturation in the low-permeability zone before the permeability change, as shown in Figure 4.16 and Figure 4.17. As ∇P_3^{LH} drops at around 0.75 PVI surfactant, the build-up in gas is released and S_w in the low-permeability zone averages about 35% through the rest of the experiment, as shown in the corresponding CT images.

In this experiment, we are operating at conditions unfavourable, but close to, the critical conditions required for foam generation predicted theoretically (Rossen 1999). However, the CT images and the pressure measurements provide strong evidence of foam generation at the permeability contrast and its subsequent propagation downstream.

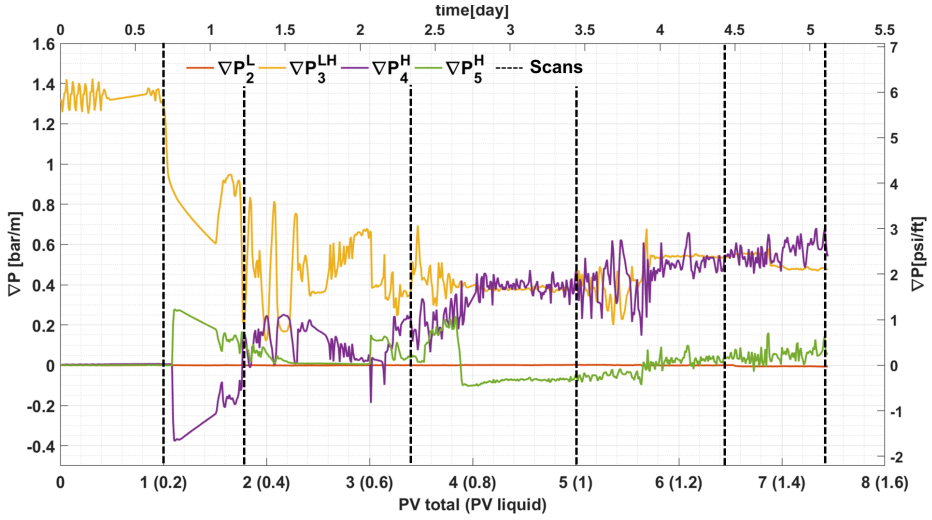

Figure 4.12: *Pressure gradient profile at superficial injection velocity 0.67ft/day (qt=0.1ml/min) and fg=80%.*

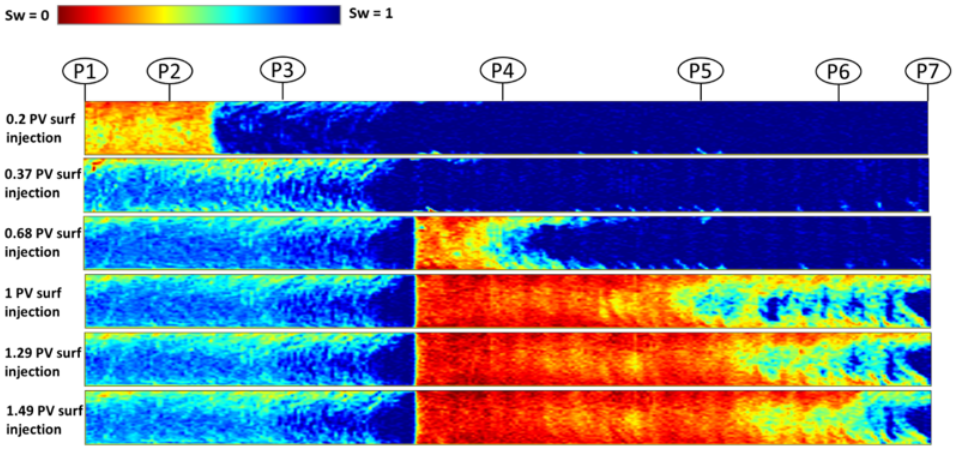

Figure 4.13: *2-Dimensional CT imaging in the center of core as seen in vertical cross section. Blue illustrates as liquid saturation and red illustrates as gas saturation. CT scan is taken in every volume liquid injection at superficial injection velocity 0.67 ft/day (flowrate 0.1ml/min) and fg = 80%.*

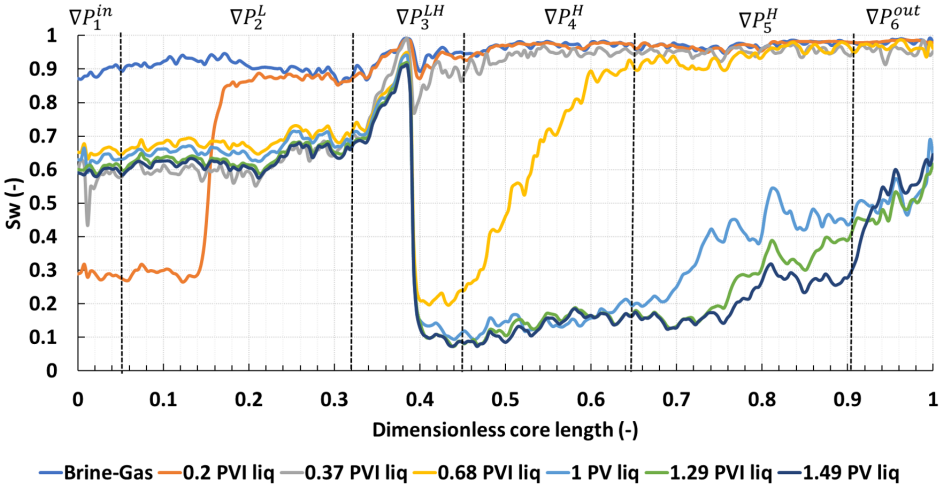

Figure 4.14: *Saturation profile along core section at injection velocity 0.67ft/day (0.1ml/min) and fg=80%.*

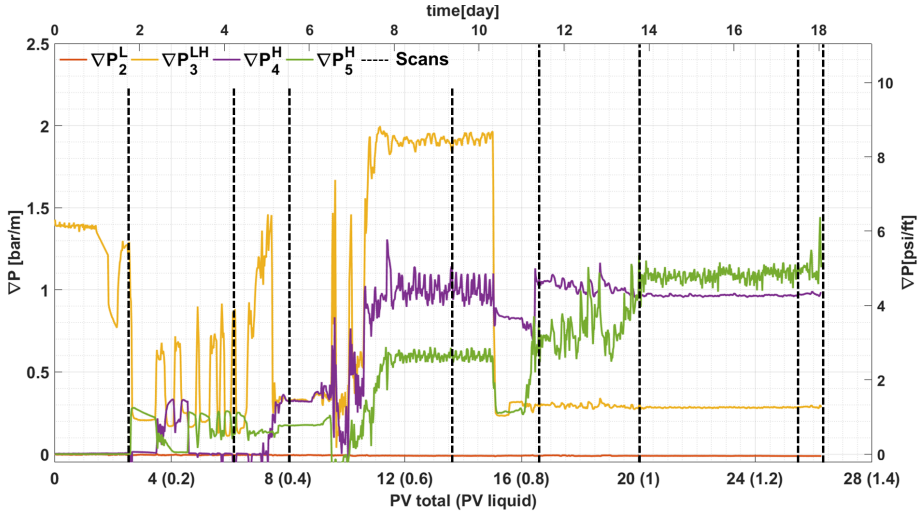

Figure 4.15: *Pressure gradient profile at superficial injection velocity 0.67ft/day (qt=0.1ml/min) and fg=95%.*

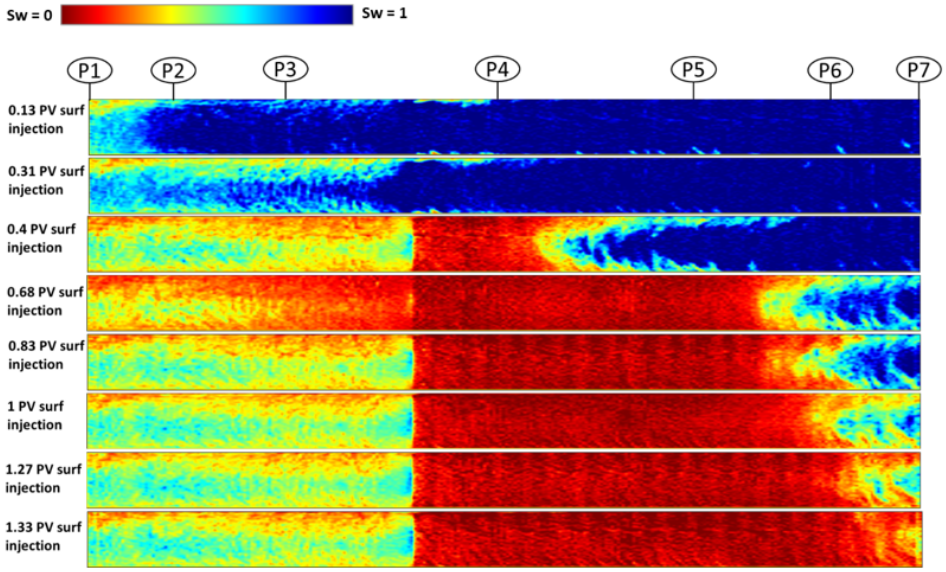

Figure 4.16: *2-Dimensional CT imaging in the center of core as seen in vertical cross section. Blue illustrates as liquid saturation and red illustrates as gas saturation. CT scan is taken in every volume liquid injection at superficial injection velocity 0.67 ft/day (flowrate 0.1ml/min) and fg = 95%.*

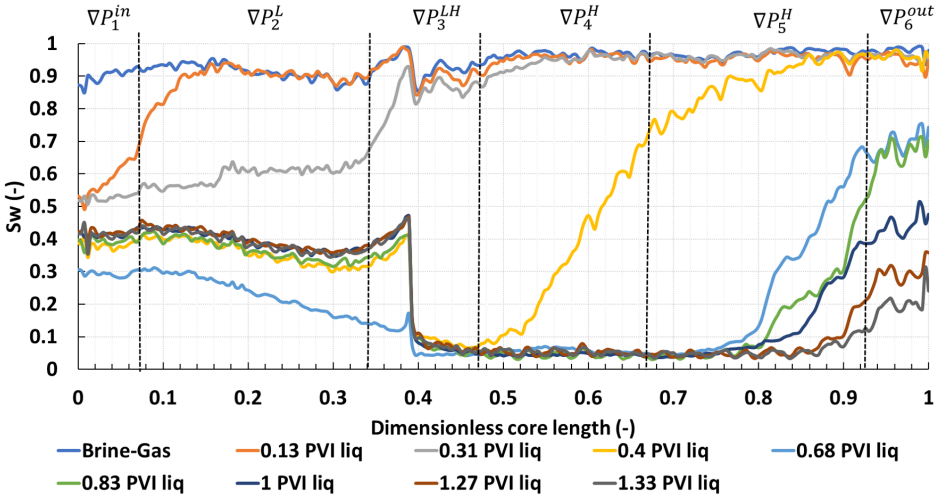

Figure 4.17: *Saturation profile along core section at injection velocity 0.67ft/day (0.1ml/min) and fg=95%.*

5

Discussion

In this study, we successfully performed experiments in which foam generation by capillary snap-off in flow across a permeability contrast was observed at different injection velocity and gas fractional flow. We chose to use a synthetic sintered-glass porous medium, with the objective of avoiding the edge effect that Li *et al.* (2005) reported as being the reason for not observing foam generation in their experiments. However, imperfect sintering of the glass grains with the tube walls resulted in a region of approximately 2-3% higher porosity near the edges of the core. As a result, gas breakthrough was observed more quickly than expected. Despite these unwanted effects, foam generation was still observed across the permeability jump, as shown by the CT measurements. Foam appears to travel faster along the edges compared to the central part of the core due to this defect.

As reported in Chapter 4, CT images (in for example, Figure 4.9 and Figure 4.13) show a relatively high gas saturation in the inlet section, at the beginning of co-injection of surfactant and gas. This shows up only in the first CT image taken after the introduction of surfactant into the core and disappears in the subsequent images. In Figure 4.13, the CT image at 0.2 PVI surfactant shows a region, roughly measuring a tenth of the core length, with a gas saturation of ≈75%. While a high gas saturation may be the typical response for foam, in this case, pressure measurements (red line or ∇P_2^L in Figure 4.12) do not indicate any significants reduction in gas mobility. In Figure 4.16, CT images show, on average, a gas saturation of 65% across the low-permeability section. Once again, the pressure measurements (∇P_2^L) in Figure 4.15 does not rise significantly in response to this build-up in gas saturation. This means that the high gas saturation in the low-permeability section, in these experiments, is not a trigger for foam generation across the permeability change downstream of the build-up. As explained in the previous chapter, the rise in (∇P_2^L) may be due to the formation of a weak leave-behind or continuous-gas foam that does not offer much resistance to the flow of gas, or due to mobilization of any gas trapped in the inlet end-cap.

5.1. Foam Generation and Propagation

Capillary Snap-off. As explained at Section 2.4, snap-off happens when capillary pressure drops to certain value (P_c^{sn}) at the boundary in the low-permeability section. The experiments of Falls *et al.* (1988) showed that P_c^{sn} is approximately equal to one half of the entry pressure ($P_c^{sn} \approx P_c^e/2$). Figure 5.1a shows the capillary pressure curve for the fine-grained (blue line) and the coarse-grained (red line) sections, based on the Laverett J-function measured for similar cores by Berg *et al.* (2014). Figure 5.1b illustrates the steady-state water-saturation profile when gas and brine flow through core 1 (k^H/k^L = 3.8:1). The capillary-pressure curves for the sintered-glass porous medium can be extended to intersect with the vertical line representing a water-saturated core (S_w = 1) to obtain an approximate capillary entry-pressure for the medium. Figure Figure 5.1a shows $P_c^e \approx$0.079 bar and therefore $P_c^{sn} \approx$0.039 bar.

We use the approach of van Lingen (1998) and Yortsos and Chang (1990) to follow the saturation path across the permeability jump along the capillary-pressure curve. When gas and liquid are flowing past the heterogeneity boundary, liquid phase (wetting phase) accumulates (S_w at B, Figure 5.1b) at the upstream side of boundary as capillary pressure falls to maintain capillary equilibrium with the high-permeability zone. At the entrance of the high-permeability zone, the saturation abruptly drops, close to its value in the bulk of the low-permeability section (S_w at C, Figure 5.1b). Based on the water-saturation profile in Figure 5.1b, we can find that capillary pressure at the end of the low-permeability zone (when the liquid phase accumulates at the permeability change) is lower than the capillary pressure for snap off: P_c at B = 0.026 bar (S_w = 0.98) and P_c^{sn} = 0.039 (S_w = 0.96). Therefore, this condition complies with the snap-off requirement.

Figure 5.2a illustrates the capillary pressure when surfactant solution is present in the core and foam is starting to be generated at the permeability jump. The capillary pressure is lower than in Figure 5.1a as the surface tension is lowered. Lamellae created by snap-off become more stable in the presence of surfactant, and strong foam is formed downstream of the permeability contrast. Figure 5.2b shows that water saturation drops abruptly as foam generation dries out the region (at S_w = C) and foam propagates downstream.

Effect of Injection Velocity. Figure 5.3 illustrates that a lower injection velocity results in a higher apparent viscosity, indicating shear-thinning behaviour of foam. Although the lowest injection velocity (0.025 ml/min or 0.17 ft/day) gives the highest apparent viscosity, we observe intermittent flow of foam at the outlet of the core until the end of the experiment. At a lower velocity, the fluctuation of pressure gradient and, consequently, apparent viscosity, once foam has been generated, is greater. The magnitude of these fluctuations is represented by the errorbars in Figure 5.3, which represent one standard deviation of all measurements made within a period of 0.1 PVI Liquid.

We assume a homogeneous high-permeability zone to evaluate foam propagation through the section. Tanzil (2001) reports a dimensionless capillary number (N_{cL}) to identify conditions favorable for propagation of foam in the porous medium. Above a critical dimensionless capillary number (N_{cL}^* = 2), foam

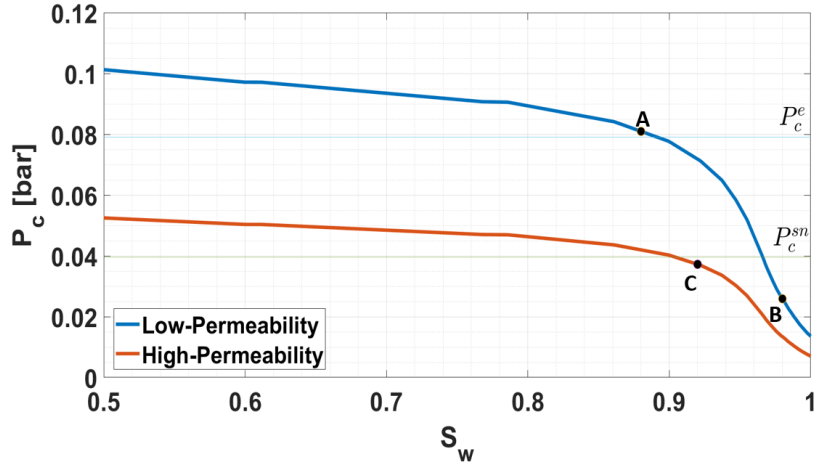

(a)

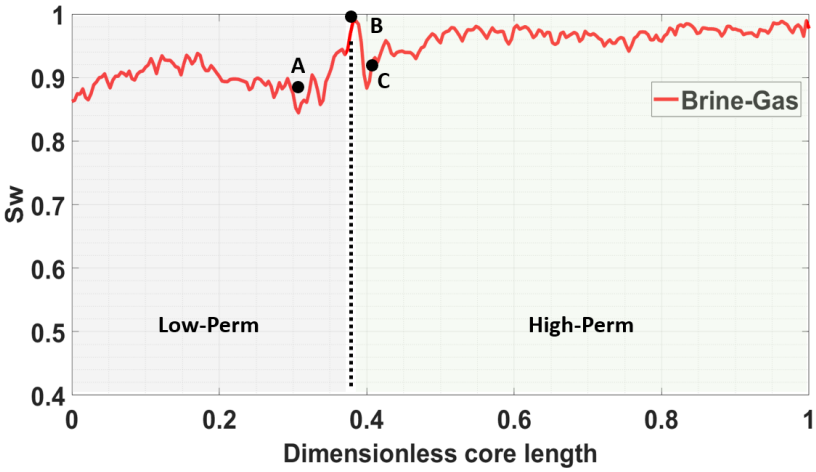

(b)

Figure 5.1: *Capillary pressure curves for the homogeneous high- and low-permeability regions in core 1 (k^H/k^L = 3.8:1) (**a**) Steady-state water-saturation profile during gas-brine co-injection (**b**).*

propagation can be expected across the region used to define the quantity. The dimensionless capillary number is defined as:

$$N_{cL} = \frac{\Delta P}{\frac{\sigma}{\sqrt{k/\phi}}} \tag{5.1}$$

where ΔP is the pressure drop (Pa), ideally calculated across "short intervals of the gas front" (Tanzil 2001). In this case ΔP is calculated over the respective section

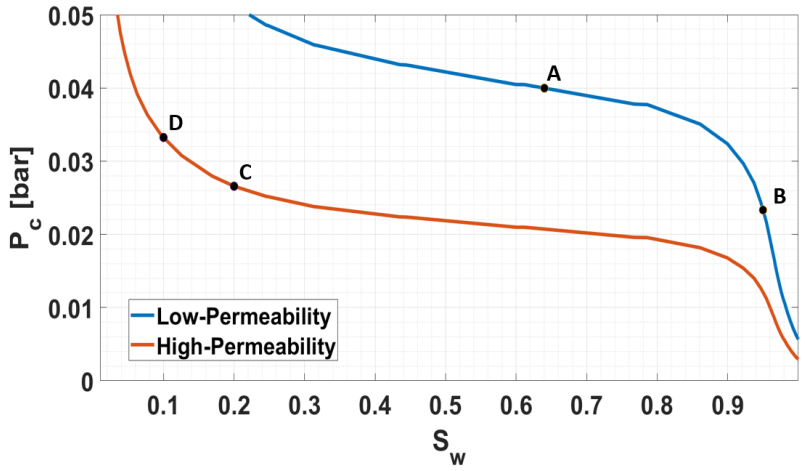

(a)

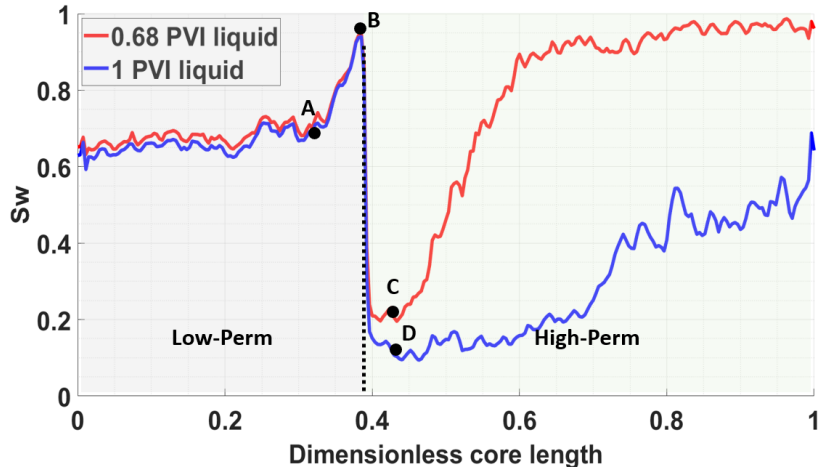

(b)

Figure 5.2: *Capillary pressure curves for the homogeneous high- and low-permeability regions in core 1 (k^H/k^L = 3.8:1) (**a**) and steady-state water-saturation profile during gas-surfactant co-injection (**b**).*

length. σ is the surface tension (N/m), k is the absolute permeability (m^2), and ϕ is the porosity (-).

Tanzil (2001) observes strong foam in his experiments with sufficient pressure gradient to mobilize the foam at a critical dimensionless capillary number (N^*_{cL}) of 2. In our experiments, the N_{cL} value in the 4th section of core (P^H_4), always exceeds the critical value (Figure 5.5). However, Figure 5.6 shows that at the lowest injection velocity (0.025 ml/min or 0.17 ft/day) it is difficult to reach N^*_{cL}~2 in the 5th section

of the core. In conclusion, foam generation is independent of the injection velocity but there is a minimum injection velocity required to ensure foam propagation to the end of the core.

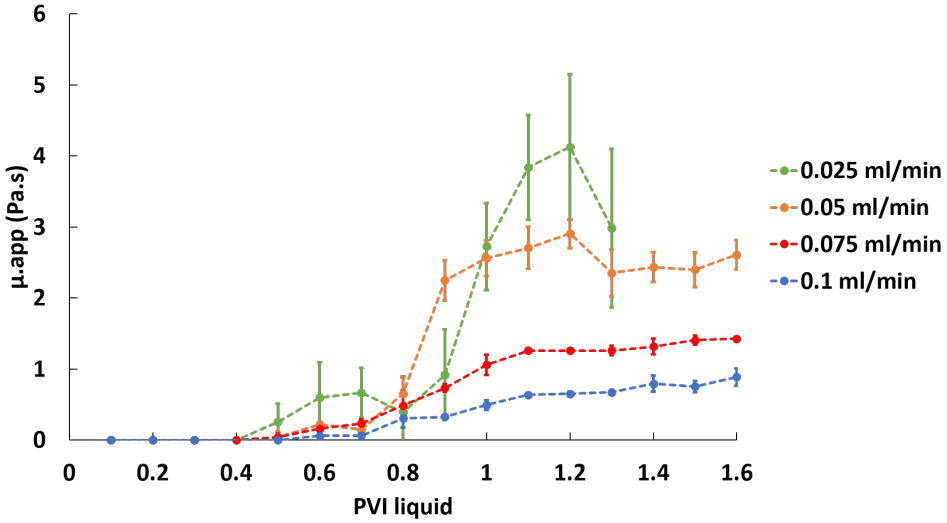

Figure 5.3: *Apparent viscosity in the high-permeability section of core 1 at 80% foam quality for different injection velocities, corresponding to Figure 5.4.*

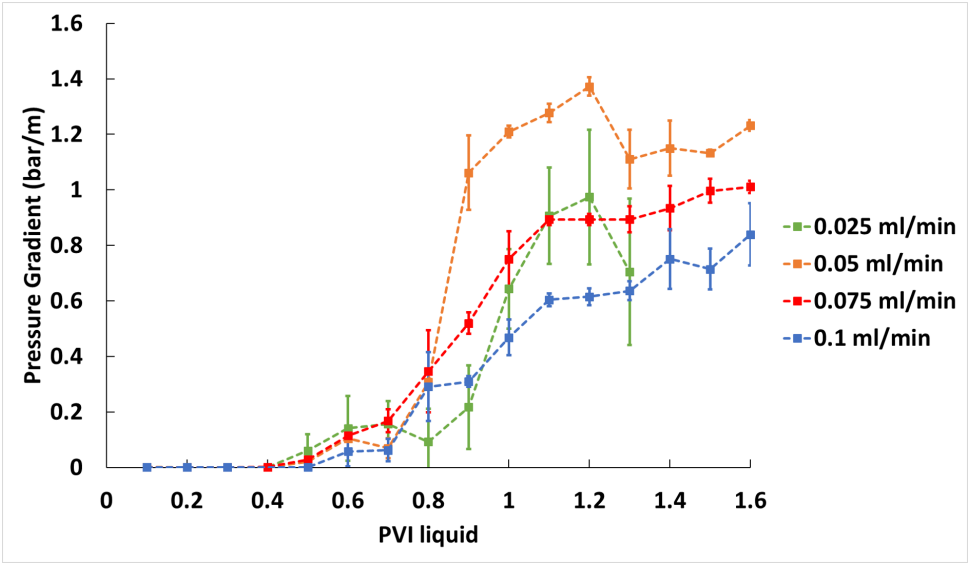

Figure 5.4: *Pressure gradient, averaged over intervals of 0.1 PVI liquid, in the high-permeability section of core 1 at 80% foam quality for different injection velocities.*

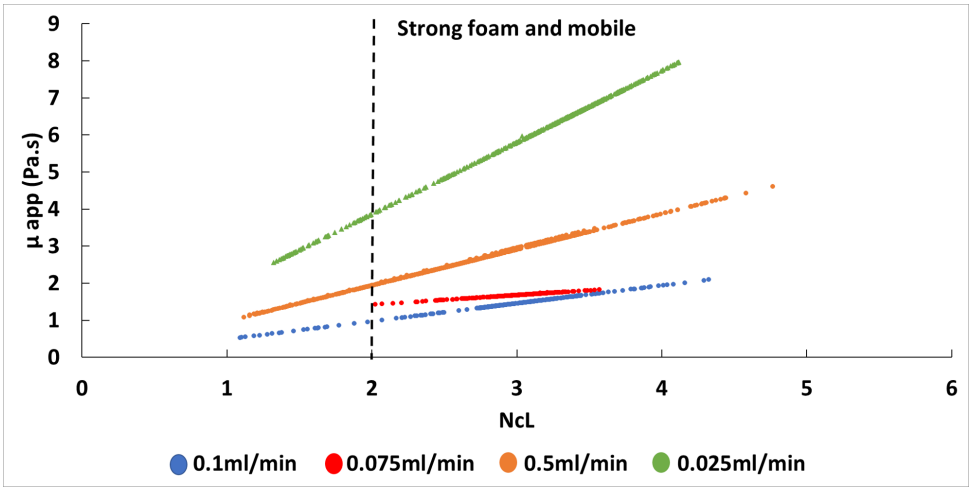

Figure 5.5: *Apparent viscosity versus N_{cL} corresponding to P_4^H in core 1 for different injection velocities.*

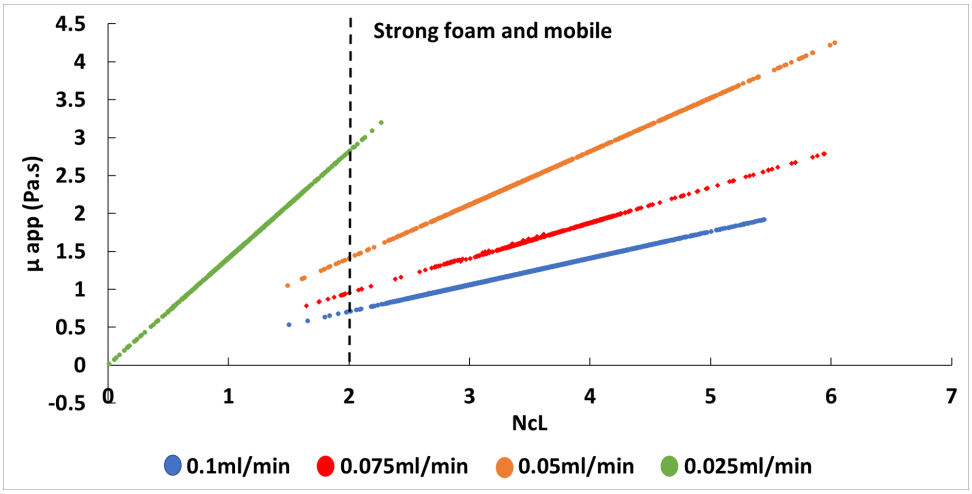

Figure 5.6: *Apparent viscosity versus N_{cL} corresponding to P_5^H in core 1 for different injection velocities.*

Effect of Foam Quality. We conduct three experiments at the same total injection velocity (0.67 ft/d) and different foam qualities (95%, 80%, and 60%). CT images clearly show that foam is generated at the permeability contrast and it propagates to end of the core for different foam qualities. Figure 5.7 shows the average pressure gradient in each section of the core as measured over the last 0.2 PVI surfactant of each experiment conducted at the three different fractional flows. Figure 5.8 shows the pressure gradient in the high-permeability section through the course of these three experiments performed in the CT scanner. The core is placed horizontally. At a higher gas fraction, a greater reduction in gas mobility is

achieved. We did not expect to see foam generation at the high gas fraction of 95% with a permeability contrast of 3.8:1, in accordance with Figure 2.5. However, CT images in Figure 4.16 confirm that foam is generated at this high foam quality at the permeability transition and Figure 5.8 shows that the foam is stronger at f_g = 95% compared to f_g = 60% and f_g = 80%. This suggests that at f_g = 95%, we are still operating in the low-quality regime. Foam generation also appears to occur after a longer period of liquid injection when the flow is wetter. In other words, when plotted against PVI liquid, pressure gradient in the high-permeability section rises first in the experiment conducted at f_g = 95% and last in the experiment conducted at f_g = 60%.

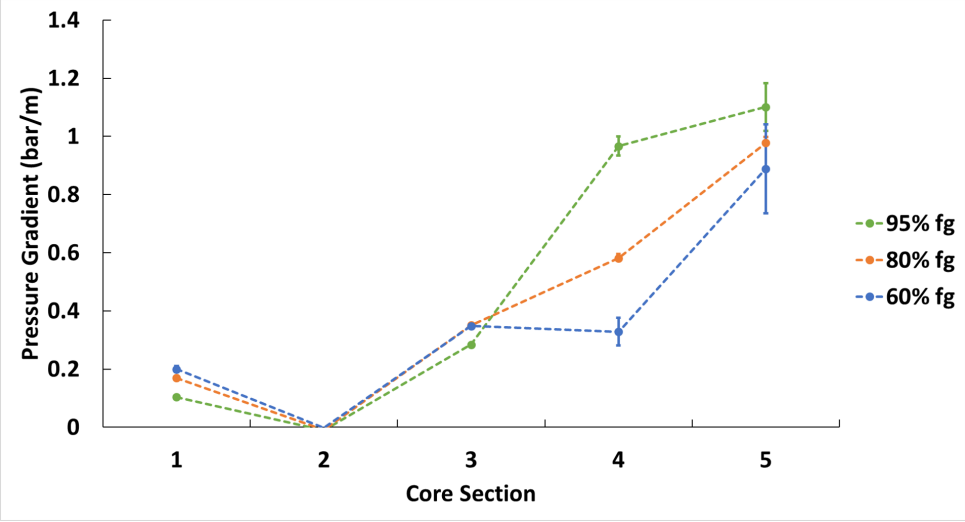

Figure 5.7: *Pressure gradient profile along the horizontal core at different fractional flow averaged through the last 0.2 PVI of surfactant injection.*

The same experiment performed with the core placed vertically does not appear to follow this trend, as shown in Figure 5.9. Foam generation is observed after roughly the same amount of liquid injection. In the early stages of the experiment, roughly the same pressure gradient is observed at different f_g. However, at the end of the experiment, when the pressure gradient fluctuates around the same steady-state value, it appears that the highest apparent viscosity of the foam is achieved at f_g = 80%, followed by f_g = 60% and f_g = 95%. This is consistent with foam-scan experiments conducted with the same high-permeability sample as shown in Appendix B.

These results do not coincide with observations made in previous work. The experiments of Falls *et al.* (1988) at different foam quality showed a lower pressure drop at gas fractional flows (foam quality) larger than 80%. They reported that lamellae were steadily created when the foam quality was lower than 80% and intermittent lamella generation was observed at higher qualities. These observations align with the experiments of Tanzil *et al.* (2002a), who observed

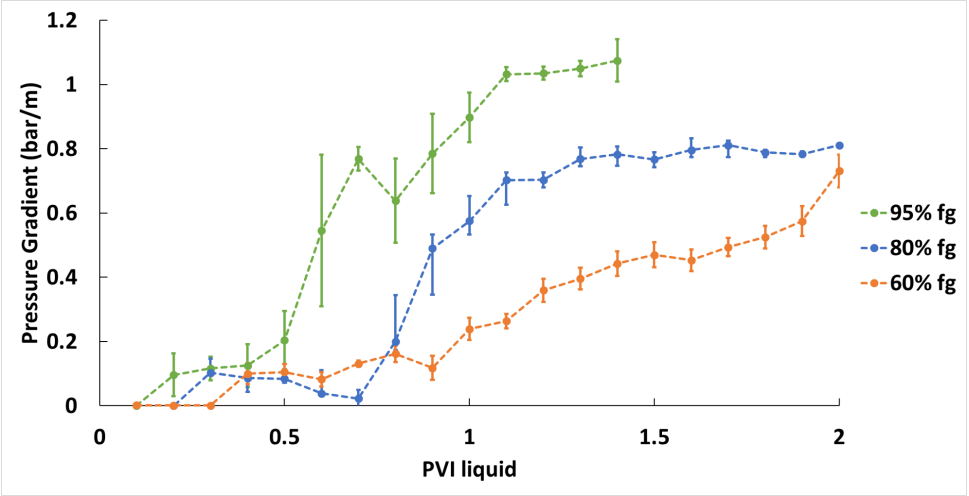

Figure 5.8: *Pressure gradient in the high-permeability zone during the foam-generation experiments conducted in core 1 (k^H/k^L = 3.8:1) with the core placed horizontally. The experiments were conducted at a total injection velocity of 0.67 ft/day and three different injection fractions.*

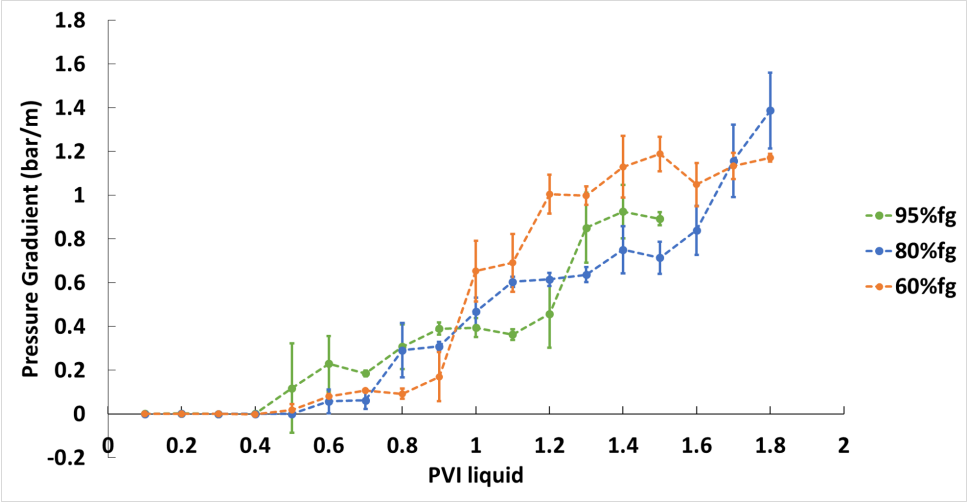

Figure 5.9: *Pressure gradient in the high-permeability zone during the foam-generation experiments conducted in core 1 (k^H/k^L = 3.8:1) with the core placed vertically. The experiments were conducted at a total injection velocity of 0.67 ft/day and three different injected gas fractions.*

that strong foam was generated at gas fractions less that 87% and the rise in pressure gradient was slower, and its magnitude was lower, at f_g = 95%. The experiments of Falls *et al.* (1988) and Tanzil *et al.* (2002a) were both performed with the core placed horizontally, and with a greater permeability contrast compared to our experiments (4.4:1 for the experiments of Tanzil *et al.* (2002a) and ≈14:1-25:1

for the experiments of Falls *et al.* (1988)). The difference in results between our experiments and previous experiments can be explained by the fact that Falls and Tanzil conducted their experiments under drainage conditions. In their experiments, gas was injected into a surfactant-saturated core to observe foam generation across a sharp permeability jump. In our experiments, gas and surfactant solution were injected simultaneously into a medium at steady-state with gas and brine injection.

Gravity segregation. Foam can reduce the extent of gravity segregation by effectively reducing the mobility of gas in the vertical direction. In a layered system, foam can be generated by snap-off due in flow across layer boundaries. Foam would then plug the upper layers and restrict further upward movement of gas. We apply VGR (Viscous Gravity Ratio) to predict the extend of gravity segregation in our core (Shi and Rossen 1998):

$$\mathrm{VGR} = \frac{k_h h}{k_v L} \frac{\nabla P}{\Delta \rho g} \tag{5.2}$$

The dimensionless $\frac{k_h h}{k_v L}$ is the reservoir aspect ratio and $\frac{\nabla P}{\Delta \rho g}$ is the inverse of the gravity number. The simulation of Shi and Rossen (1998) classify the type of gravity override based on VGR value:

- no override, if the foam front is piston like,
- Incipient override, if foam fills 40% to 50% of reservoir volume but lags the expected piston-like displacement.
- Moderate override, if foam fills 10% to 40% of reservoir volume with VGR value 0.1 to 0.4,
- Severe override, if the foam invades less than 10% of reservoir volume with VGR value < 0.1.

Based on above of classification, Table 5.1 shows that severe gravity override would be expected for co-injection gas and brine. Foam generation in the high-permeability section (downstream of permeability contrast) increases the VGR value significantly. Therefore, it proves that foam generation in this experiment can help solve the gravity override problem.

5

Table 5.1: *Viscous Gravity Ratio in the horizontal core experiment*

Experiment	VGR value at Low-Perm Section		VGR value at High-Perm Section	
	Gas-Brine*	Gas-Surfactant**	Gas-Brine*	Gas-Surfactant**
0.1 ml/min 95%fg	6.8e-02	0.05	1.2e-03	1.59
0.1 ml/min 80%fg	7e-02	0.10	7e-04	1.28
0.1 ml/min 60%fg	8.7e-02	0.13	1e-03	1.0

* average at gas-brine injection
** average after foam generation

6

Conclusions and Recommendations

In this experimental study, we successfully show that foam can be generated by capillary snap-off in flow across sharp permeability contrasts. This process is shown to be independent of applied pressure gradient or velocity and relies solely on the contrast in capillary pressure across two regions as predicted by Rossen (1999). We investigated the effect of injection velocity on this process to try to verify this within practically possible limits. A wide range of injection velocities and gas fractions that resulted in foam generation and propagation to the end of the core were identified, as shown in Figure A.1. Even at velocities as low as 0.17 ft/day (f_g = 80%) for core 1 (k^H/k^L = 3.8:1) and (f_g = 95%) for core 2 (k^H/k^L = 14:1), foam generation was observed across the permeability jump. However, in these two cases, foam did not propagate beyond the first section in the high permeability zone. Small periods of foam production were observed at the outlet, unlike other experiments, where typically only foam was produced at the outlet.

Our experiments were accompanied by relatively large fluctuations in pressure gradient once foam generation began. We attribute this behaviour to the intermittency of this process (Falls *et al.* 1988, Shah *et al.* 2018). Foam is not generated steadily as surfactant and gas flow across the permeability transition. Instead, there are periods of foam generation, which lead to short intervals of drier flow, which increase the local capillary pressure to a value above P_c^{sn}. Until liquid imbibes back or convects to the boundary of the low-permeability region, foam generation ceases. Following the arrival of liquid, as liquid accumulates at the boundary of the low-permeability zone and P_c drops below P_c^{sn} again, foam generation recommences. Depending on the velocity and the local flowing gas fraction and permeability contrast Shah *et al.* (2018), the duration of the foam-generation interval may be much larger than, or comparable to, the duration of the no-foam-generation interval. With the current setup for our experiments,

the individual, periodic events of generation and no generation are too frequent to detect. However, on a larger time-scale, they show up as fluctuations in the local pressure gradient, which we can use to comment on the intermittency of this process as injection velocity and gas fraction changes. In our experiments, as the injection velocity was reduced, the magnitude of pressure fluctuations increased. Across the permeability jump, as the injection velocity was reduced, the observed pressure gradient during foam generation was also higher.

We also performed experiments to verify the theoretical limits of this phenomenon with respect to gas fractional flow. In the model of Rossen (1999), it was shown that foam generation across a permeability contrast of 4:1 may be difficult beyond a flowing gas fraction of 80%. However, in our experiments, foam generation and propagation was observed at a permeability contrast of approximately the same magnitude but a much higher gas fraction of 95%. The CT results help verify that foam is indeed generated at the permeability contrast and from there on it propagates downstream to the outlet of the core. In terms of phase saturations, there is no clear difference in the high-permeability zone with changing f_g. However, in the low-permeability zone, a higher gas saturation is observed at higher f_g. While this may appear to be foam based on purely the CT results, the pressure measurements do not indicate any major reduction in gas mobility, and this suggests that the accumulation of gas in any part of the low-permeability zone is most likely a result of the formation of weak or continuous-gas foam or due to the mobilisation of any trapped gas present in the inlet end-cap. Pressure measurements from the three experiments at constant velocity and different gas fractional flow also show that the reduction in gas mobility is greater at a higher gas fractional flow as shown in Figure 5.8. This is in contrast to previous studies (Falls *et al.* 1988, Tanzil *et al.* 2002b), which were performed under drainage conditions as discussed in Chapter 5.

We expected to see foam generation as soon as the liquid front reaches the permeability contrast in the core. In other words, we expected foam generation to occur after the same number of pore volumes of liquid injected at varying f_g in our experiments. However, we did not observe this when the core was placed horizontally in the CT machine. No clear relation was observed with the amount of liquid injected and the onset of foam generation. When the same set of experiments were performed with the core placed vertically, the onset of foam generation and its arrival into the high-permeability zone occurred after roughly the same amount of surfactant had been injected into the core. This difference in results with change in core orientation is most likely due to gravity segregation in the low-permeability section (when the core is placed horizontally) affecting the time at which the fluids arrive at the permeability contrast.

As mentioned before, our experiments were performed using a sintered glass core, in order to minimize the edge effect, which leads to a region of higher porosity near cylindrical walls of the core compared to its central region, and to ensure a consolidated nature of the porous medium in order to avoid any grain migration from affecting the foam-generation process. Unfortunately, we still observed the edge effect, perhaps even worse than the one observed by Li *et al.*

(2005) in their experiments. Despite this, we observed foam generation across the permeability contrast under conditions elaborated in previous chapters. Due to the non-uniform porosity, in the CT images, as illustrated in chapter 5, foam generation and propagation appears to be faster near the walls of the core. All the CT images taken after the onset of foam generation show that the high-gas-saturation region (in red) has traveled further along the edges of the core compared to the center of the core, as seen in a vertical slice through the middle of the core. Therefore, as a recommendation for future work, we propose that similar experiments be performed with a layered core having more homogeneous, individual sections. Recently van Ballaer (2018) developed a method for successfully creating homogeneous, compacted, well-characterized and well-consolidated layered sandpacks. If we compare with sintered glass core (Figure 6.1b), his sandpacks do not suffer from the same artifact at the edges as shown in Figure 6.1a and may be an ideal candidate for performing similar experiments. Moreover, since reservoir rocks are usually made of the same material, the use of sand brings the experimental conditions closer to reservoir conditions. One can more accurately understand the impact of surfactant adsorption on this process and obtain realistic estimates of the the amount of surfactant required to generate foam across a sharp permeability contrast. Further, the same study must be performed in the presence of oil to establish if strong foam can still be generated through this phenomenon in the presence of residual oil. It may be interesting to see if this foam helps reduce oil saturation in the downstream high-permeability sections. When investigating the impact of oil on foam generation, different surfactants (compatible with the oil used) must also be tested as they may impact the foam-generation process.

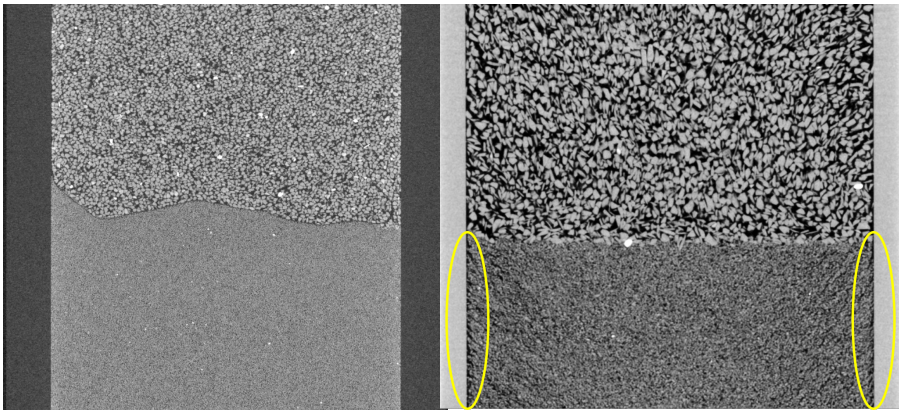

(a) ***(b)***

Figure 6.1: *Layered sandpack, compacted using a centrifuge at 150g (van Ballaer 2018) (**a**). Layered sintered glass core (**b**).*

7

References

L. W. Lake *et al.*, *Fundamentals of enhanced oil recovery* (Society of Petroleum Engineers, 2014).

W. R. Rossen, *Foams in enhanced oil recovery,* in *Foams: theory, measurements and applications*, Vol. 57 (Marcel Dekker, New York, 1996) pp. 413–464.

P. A. Gauglitz, F. Friedmann, S. I. Kam, and W. R. Rossen, *Foam generation in homogeneous porous media,* Chemical Engineering Science **57**, 4037 (2002).

T. Ransohoff and C. Radke, *Mechanisms of foam generation in glass-bead packs,* SPE reservoir engineering **3**, 573 (1988).

D. Tanzil, G. J. Hirasaki, and C. A. Miller, *Conditions for foam generation in homogeneous porous media,* in *SPE/DOE Improved Oil Recovery Symposium* (Society of Petroleum Engineers, 2002).

A. Falls, G. Hirasaki, T. Patzek, D. Gauglitz, D. Miller, T. Ratulowski, *et al.*, *Development of a mechanistic foam simulator: the population balance and generation by snap-off,* SPE Reservoir Engineering **3**, 884 (1988).

W. R. Rossen, *Foam generation at layer boundaries in porous media,* SPE Journal **4**, 409 (1999).

D. Tanzil, G. J. Hirasaki, and C. A. Miller, *Mobility of foam in heterogeneous media: Flow parallel and perpendicular to stratification,* SPE Journal **7**, 203 (2002b).

J. Bikerman, *Foams*, Vol. 1 (Springer Science & Business Media, 1973).

W. R. Rossen, *Theories of foam mobilization pressure gradient,* in *SPE Enhanced Oil Recovery Symposium* (Society of Petroleum Engineers, 1988).

W. R. Rossen, *A critical review of roof snap-off as a mechanism of steady-state foam generation in homogeneous porous media,* Colloids and Surfaces A: Physicochemical and Engineering Aspects **225**, 1 (2003).

D. Tanzil, *Foam generation and propagation in heterogeneous porous media*, Ph.D. thesis, Rice University (2001).

Y. C. Yortsos and J. Chang, *Capillary effects in steady-state flow in heterogeneous cores,* Transport in Porous Media **5**, 399 (1990).

A. Falls, J. Musters, J. Ratulowski, *et al.*, *The apparent viscosity of foams in homogeneous bead packs,* SPE Reservoir Engineering **4**, 155 (1989).

Q. Li, W. R. Rossen, *et al.*, *Injection strategies for foam generation in homogeneous and layered porous media,* in *SPE annual technical conference and exhibition* (Society of Petroleum Engineers, 2005).

C. A. Hartkamp-Bakker, *Permeability heterogeneity in cross-bedded sandstones: Impact on water/oil displacement in fluvial reservoirs*, Ph.D. thesis, Delft University of Technology (1993).

K. Weber *et al.*, *Influence of common sedimentary structures on fluid flow in reservoir models,* Journal of Petroleum Technology **34**, 665 (1982).

W. V. D. G. P. Ealey, *Geological modeling for simulation studies,* AAPG Bulletin **73**, 1436 (1989).

S. Y. Shah, K.-H. Wolf, R. M. Pilus, and W. R. Rossen, *Foam generation by capillary snap-off in flow across a sharp permeability transition,* in *SPE Improved Oil Recovery Conference* (Society of Petroleum Engineers, 2018).

R. Farajzadeh, R. Krastev, and P. Zitha, *Foam films stabilized with alpha olefin sulfonate (AOS),* Colloids and Surfaces A: Physicochemical and Engineering Aspects **324**, 35 (2008).

B. C. Sharma, W. E. Brigham, L. M. Castanier, and T. Reid, *CT imaging techniques for two-phase and three-phase in situ saturation measurements,* Prepared for U.S. Department of Energy, Assistant Secretary for Fossil Energy (1997).

M. Simjoo, *Immiscible Foam for Enhancing Oil Recovery*, Ph.D. thesis, Delft University of Technology (2012).

C. S. McCool, R. Parmeswar, and G. P. Willhite, *Interpretation of differential pressure in laboratory surfactant/polymer displacements,* Society of Petroleum Engineers Journal **23**, 791 (1983).

X. Chen, A. Kianinejad, and D. A. DiCarlo, *An extended jbn method of determining unsteady-state two-phase relative permeability,* Water Resources Research **52**, 8374 (2016).

S. Berg, R. Armstrong, H. Ott, A. Georgiadis, S. Klapp, A. Schwing, R. Neiteler, N. Brussee, A. Makurat, L. Leu, *et al.*, *Multiphase flow in porous rock imaged under dynamic flow conditions with fast x-ray computed microtomography,* Petrophysics **55**, 304 (2014).

P. van Lingen, *Quantification and reduction of capillary entrapment in cross-laminated oil reservoirs*, Ph.D. thesis, Delft University of Technology (1998).

J. Shi and W. R. Rossen, *Simulation of gravity override in foam processes in porous media,* SPE Reservoir Evaluation & Engineering **1**, 148 (1998).

A. van Ballaer, *Petrophysical characteristics of a compressed sand pack*, Master's thesis, Delft University of Technology (2018).

Nomenclature

A	Cross section of core [m^2]
CT	Xray CT measurements [HU]
dn/dt	Number of moles injected per unit time [mol/s]
dP/dt	Pressure over time [bar/s]
F	Force [N]
f_g	Gas fractional flow [-]
k	Absolute permeability [m^2]
L	Length of core [m]
N_{cL}	Capillary number [-]
P	Pressure [bar]
P_c	Capillary pressure [bar]
ΔP	Pressure drop [bar]
∇P	Pressure gradient [bar/m]
q	Flowrate [ml/min]
R	Ideal gas constant [L bar $K^{-}1$ $mol^{-}1$]
S	Saturation [-]
T	Temperature [K]
u	Superficial (Darcy) velocity [m/s]
V_m	Volume molar [L/mol]
σ	Interfacial tension [N/m]
μ	Viscosity [Pa.s]
ϕ	Porosity [-]

Supercripts

e	entry, used to denoted capillary entry pressure
L	Low-permeability region
LH	Low- to high-permeability region
H	High-permeability region
sn	snap-off, used to denoted capillary pressure for snap-off
t	total

Subscripts

app	Apparent
am	CT attenuation of the dry core
foam	CT attenuation of experiment
g	Gas
l	Liquid
w	Water
wm	CT attenuation of water saturated core

A

Foam Generation and Propagation

We have performed a series of the experiments at different values of injection velocity and gas fractional flow as described in table 3.4. Figure A.1 shows the qualitative results for foam generation and propagation as function of permeability contrast, injection velocity, and gas fractional flow. The data are combined with the experiment results of Shah *et al.* (2018).

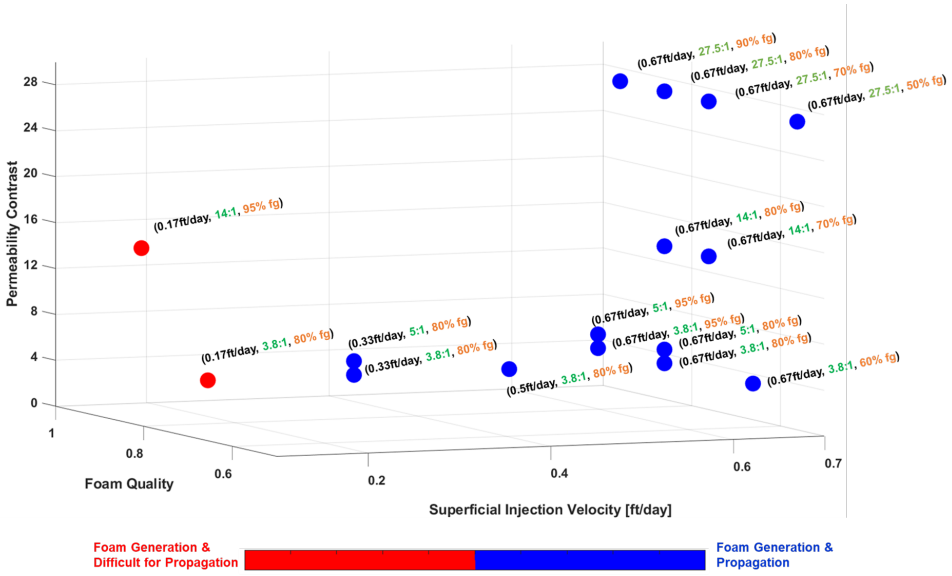

Figure A.1: *Series of Experiment Results. Data label: injection velocity, permeability contrast, foam quality*

B

Foam-Scan Experiment

This experiment is conducted to study foam flow behavior by measuring apparent viscosity at different values of fractional flow. Theoretically, there are two regimes in foam flows through porous media: the low-quality flow regime and high-quality flow regime. Apparent viscosity decreases when foam quality increases in the high-quality flow regime; it reflects dry foam and it is at relatively large superficial velocity of gas and small superficial velocity of liquid. The low-quality regime is at lower superficial velocity of gas and larger velocity of liquid. It is markedly shear-thinning; bubble trapping and mobilization dominate the foam flow (Rossen and Wang 1999). The transition between the low-quality regime and high-quality regime occurs at f_g^*.

As continuation of previous experiments, we utilize a homogeneous sintered glass core that has similar absolute permeability with high-permeability section of Core A (20 darcy). It is placed vertically, with injection from bottom to the top of the core. The core (Figure B.1) has 5 sections (ΔP_1 - ΔP_5); we focus to the middle section of core (ΔP_3) to avoid inlet and outlet effects on the steady state measurements. In this experiment, the core-cleaning procedure is conducted between every foam quality point to ensure there is no gas trapped in the core after one experiment has finished.

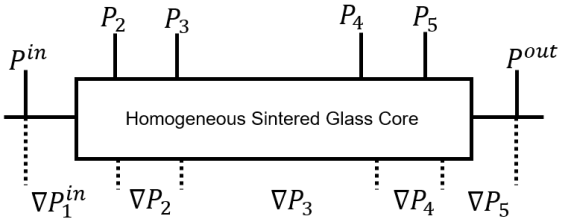

Figure B.1: *Schematic of foam-scan experiment core.*

It was difficult to achieve a stable pressure gradient in this experiment. Additionally, we conducted this experiment with low injection velocity of 0.67ft/day (0.1ml/min). The fluctuations of pressure gradient, for instance, are shown in the Figure B.2a at injection velocity of 0.67ft/day (0.1ml/min) fg=80%, and Figure B.2b at fg=90%. There are two interpretations that might represent the average value of pressure gradient, the red arrow is taken in the roughly 1-2 PV before end of the experiment and the black arrow represents a longer period of foam injection. Black-arrow data are called interpretation 1 and red-arrow data is interpretation 2.

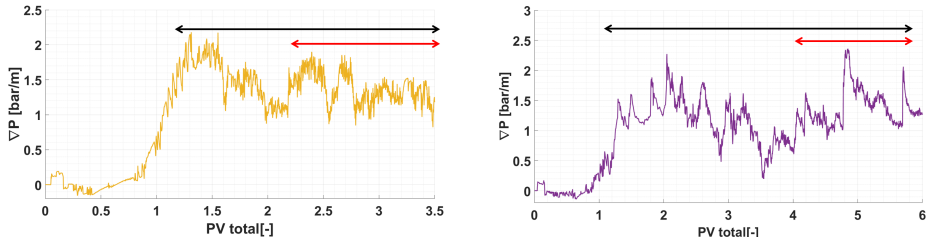

(a) ***(b)***

Figure B.2: *Pressure-gradient profile at 80%fg (**a**) and 90%fg (**b**).*

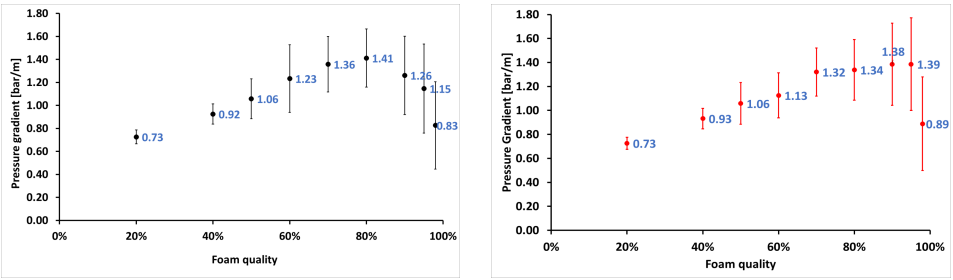

(a) ***(b)***

Figure B.3: *Pressure-gradient vs foam quality; error bars represent the fluctuation of pressure gradient. Interpretation 1 has gradually decreasing of pressure gradient after 80% of gas fractional flow (**a**) and Interpretation 2 has an abrupt drops in pressure-gradient at 95% of foam quality (**b**).*

We observe two different interpretations as result of using different ranges of the average value of pressure gradient in the experiment. The 1st interpretation (Figure B.3a) shows two distinctive foam flow regimes (error bars illustrate the fluctuation of pressure gradient); low-quality regime and high-quality regime. The transition of low-quality regime and high-quality regime occurs at 80% gas fractional flow with a maximum pressure gradient 1.41 bar/m. The 2nd interpretation (Figure B.3b) shows abruptly decreasing of pressure gradient at 95% of foam quality, with a different transition foam quality between low-quality regimes and

high-quality regimes at fg=90% and pressure gradient = 1.39 bar/m.

B.1. Foam-Model Parameters

We utilize both interpretations to measure the foam-model parameters. This study utilizes the parameters in a foam simulator, STARS. The foam simulator in STARS use a function FM, which controls the gas mobility reduction in presence of foam (Boeije and Rossen 2015):

$$u_{t,fg} = -\frac{kk^{f}_{rg}}{\mu_g}\Delta P = \frac{kk_{rg}FM}{\mu_g}\Delta P \tag{B.1}$$

$$FM = \frac{1}{1 + fmmob.F_1.F_2.F_3.F_4.F_5.F_6} \tag{B.2}$$

where k^{f}_{rg} = the gas relative permeability in presence of foam and k_{rg} = the gas relative permeability without foam. F_1 of function of surfactant concentration, F_3 of oil saturation, F_4 of gas velocity, and F_6 of critical capillary number. Functions F_2 and F_5 represent the effects of water saturation and capillary number.

This study focuses to obtains the foam-model parameters of F_2 and F_5 functions (epdry, fmdry, fmcap, epcap, and fmmob) based on experimental foam-quality scan data (Figure B.3a and Figure B.3b.

$$F_2 = 0.5 + \frac{\arctan(epdry.(S_w - fmdry)}{\pi} \tag{B.3}$$

If

$$N_{ca} > fmcap, F_5 = (\frac{fmcap}{N_{ca}})^{epcap}; \tag{B.4}$$

else,

$$F_5 = 1 \tag{B.5}$$

with,

$$N_{ca} \equiv \frac{k\nabla P}{\sigma_{wg}} \tag{B.6}$$

We use Boeije and Rossen's method to find the foam-model parameters. Parameter epdry controls the steepness of the foam collapse. Boeije and Rossen (2015)'s method assumes an abrupt transition between low and high-quality regimes. It assumes a very large value for **epdry**. Parameter fmdry is equal to water saturation (S^{*}_{w}) around which the foam collapses; epcap captures shear-thinning behavior in the low-quality regime; **fmcap** is the reference capillary pressure, and fmmob is the reference gas-mobility-reduction.

The first step to obtain the foam-model parameter is determining the foam quality transition (f^{*}_{g}) from Figure B.3a and Figure B.3b. The ∇P at f^{*}_{g} is utilized to calculate k_{rw} (S_w) by Equation B.7. Then, Corey parameter is employed to determine S^{*}_{w} or **fmdry** by use the function k_{rw} (S_w). We assume Corey parameters

for sintered glass core (Table B.1) based on glass core of Ma *et al.* (2013) and sandstone of Kapetas *et al.* (2015). The next step is to determine the value of **fmmob** using Equation B.8. To calculate epcap, we pick one point in the low-quality regime curve (not too close to f_g^*) as f_g^+. We utilize Equation B.9 to obtain the value of **epcap**. Table B.2 shows the result of foam-model paramaters using method of Boieje and Rossen.

$$u_t(1-f_g^*) = \frac{kk_{rw}(S_w^*)}{\mu_w}\nabla P(f_g^*) \tag{B.7}$$

$$\text{fmmob} = \frac{kk_{rg}(S_w^*)\nabla P(f_g^*)}{u_t f_g^* \mu_g} - 1 \tag{B.8}$$

$$\text{epcap} = \frac{\log \frac{kk_{rg}(S_w^*)\nabla P(f_g^+) - u_t f_g^+ \mu_g}{\text{fmmob} u_t \mu_g f_g^+}}{\log \frac{\nabla P(f_g^*)}{\nabla P(f_g^+)}} \tag{B.9}$$

Table B.1: *Corey parameter to calculate relative permeability.*

Parameter	Glass core 158 darcy (Ma et al., 2013)	Bentheimer 1.9 darcy (Kapetas et al., 2015)	Sintered Glass Core 20 darcy
Swc	0.07	0.25	0.08
Sgr	0	0.2	0.05
Krw	0.79	0.39	0.52
nw	1.96	2.86	2.42
Krg	1	0.59	0.59
ng	2.29	0.7	0.938

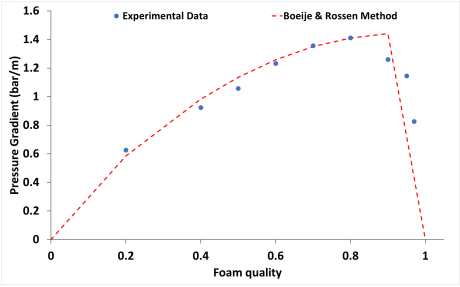

(a)

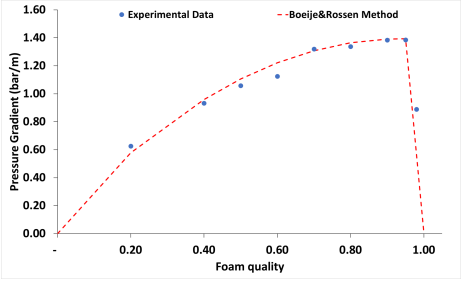

(b)

Figure B.4: *Pressure gradient vs foam quality, the graph is fitting using Boeije and Rossen's method. Interpretation 1 (***a***) and Interpretation 2 (***b***).*

Table B.2: *Foam-model parameters using Boeije and Rossen's method.*

Parameter	1st Interpretation	2nd Interpretation
fmmob	69404	72884
epdry	Inf	Inf
fmdry	0.103	0.09
fmcap	7.3E-05	7.5E-05
epcap	1.6	1.19

C

Pore Volume Calculations

As discussed at chapter 3, for pore volume-measurements use either CT image calculation and ideal gas calculations. Equation 3.2 shows the calculation to measure pore volume using the ideal gas method. Figure C.1 illustrates the pressure profile at every pressure taps when injection of N_2 over several minutes results in a straight line. The gradient of the chart represents the different of pressure over time (dP / dt) as an input for calculation. Table C.1 shows the input data for pore volume calculation. Additionally, the CT image calculation employs Equation 3.3 to obtain the porosity value. Table C.2 shows the result of pore volume calculation from CT image method and ideal gas method.

Table C.1: *Input data for pore volume calculation.*

Data	Core 1		Core 2		Core 3	
	Value	Unit	Value	Unit	Value	Unit
Flowrate	0.60	ml/min	0.30	ml/min	0.3 0	ml/min
Vm	24.79	dm^3/mol	24.79	dm^3/mol	24.79	dm^3/mol
dn/dt	4.04E-07	mol/sec	2.02E-07	mol/sec	2.02E-07	mol/sec
R	0.083	L bar/K mol	0.083	L bar/K mol	0.083	L bar/K mol
T	298.15	K	298.15	K	298.15	K
dP/dt	1.40E-04	bar/sec	6.25E-05	bar/sec	6.04E-05	bar/sec
PV	99.8	ml	80.6	ml	83.3	ml

Table C.2: *Pore volume data.*

Core	Pore Volume (ml)	
	CT Image Method	Ideal Gas Method
Core 1	99	99.8
Core 2	83	83.6
Core 3	-	80.3

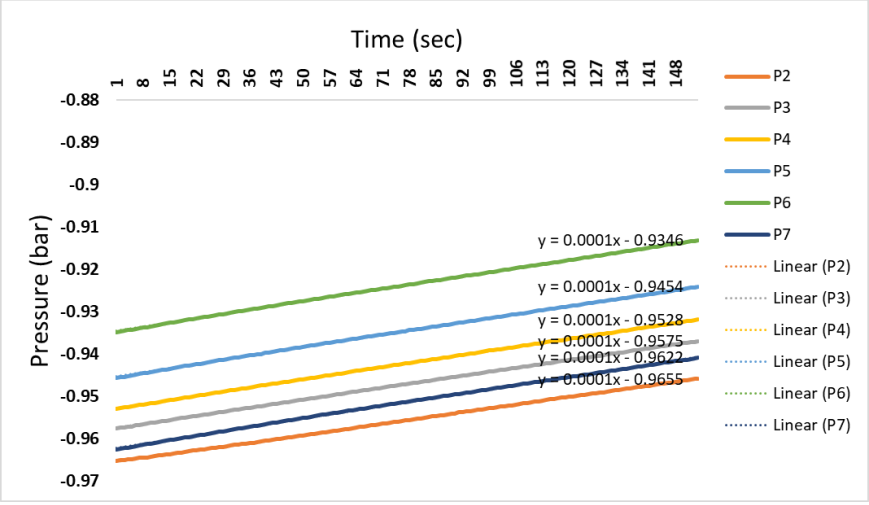

Figure C.1: *Pressure profile of core 1 in every pressure taps for N_2 injection. The injection of N_2 into a dry core over several minutes, results in a gradient of straight line chart as an input for the pore-volume calculation. Negative values of pressure occur because the N_2 injection is conducted after vacuuming the core.*

D

Absolute Permeability Result

As mention in the chapter 3, we utilize three sintered-glass cores in this experiment. Table D.1 shows the permeability value of core 1 with a permeability ratio 3.8:1 (high-permeability section: low-permeability section).

Table D.1: *Permeability data for core 1*

Permeability 1st Section	Permeability 2nd Section	Permeability 3rd Section	Permeability 4th Section	Permeability 5th Section	Permeability 6th Section
3.80 D ± 0.035 D	5.26 D ± 0.029 D	5.69 D ± 0.08 D	20.70 D ± 0.08 D	20.67 D ± 0.04 D	20.01 D ± 0.013 D

In the core 2 (Table D.2), the 1^{s}t section permeability is unexpectedly low. There may be anomalous behavior in the 1^{s}t section. But 2^{n}d section is expected permeability; transition is expected value. If the behavior into transition is as expected, then our observation at transition and downstream are acceptable. Table D.3 is the permeability value for core 3 that has permeability ratio (14:1).

Table D.2: *Permeability data for core 2*

Permeability 1st Section	Permeability 2nd Section	Permeability 3rd Section	Permeability 4th Section	Permeability 5th Section	Permeability 6th Section
1.08 D ± 0.082 D	10.25 D ± 0.043 D	20.12 D ± 0.1 D	50.03 D ± 0.412 D	56.06 D ± 0.724 D	50.25 D ± 0.08 D

Table D.3: *Permeability data for core 3*

Permeability 1st Section	Permeability 2nd Section	Permeability 3rd Section	Permeability 4th Section	Permeability 5th Section	Permeability 6th Section
3.20 D ± 0.033 D	5.13 D ± 0.054 D	7.23 D ± 0.033 D	70.15 D ± 0.02 D	70.2 D ± 0.082 D	70.31 D ± 0.01 D

Reference

S. Y. Shah, K.-H. Wolf, R. M. Pilus, and W. R. Rossen, *Foam generation by capillary snap-off in flow across a sharp permeability transition,* in *SPE Improved Oil Recovery Conference* (Society of Petroleum Engineers, 2018).

W. R. Rossen and M. Wang, *Modeling foams for acid diversion,* SPE Journal **4**, 92 (1999).

C. S. Boeije and W. Rossen, *Fitting foam-simulation-model parameters to data: I. coinjection of gas and liquid,* SPE Reservoir Evaluation & Engineering **18**, 264 (2015).

K. Ma, J. L. Lopez-Salinas, M. C. Puerto, C. A. Miller, S. L. Biswal, and G. J. Hirasaki, *Estimation of parameters for the simulation of foam flow through porous media. part 1: the dry-out effect,* Energy & fuels **27**, 2363 (2013).

L. Kapetas, S. Vincent-Bonnieu, R. Farajzadeh, A. Eftekhari, S. Mohd-Shafian, R. K. Bahrim, and W. Rossen, *Effect of permeability on foam-model parameters-an integrated approach from coreflood experiments through to foam diversion calculations,* in *IOR 2015-18th European Symposium on Improved Oil Recovery* (2015).